nature communications

Article

https://doi.org/10.1038/s41467-025-61759-1

PIP4K2C inhibition reverses autophagic flux impairment induced by SARS-CoV-2

Received: 29 July 2024

Accepted: 1 July 2025

Published online: 10 July 2025

Check for updates

Marwah Karim[1,18], Manjari Mishra[1,18], Chieh-Wen Lo[1], Sirle Saul[1], Halise Busra Cagirici[1], Manon Gourdelier[1], Luca Ghita[1], Amrita Ojha[1], Do Hoang Nhu Tran[1], Aditi Agrawal[1], Connor McGraw[1], Michael P. East[2], Karen Anbro Gammeltoft[3,4,5], Malaya Kumar Sahoo[6], Nancie A. Mooney[7], Gary L. Johnson[2,8], Soumita Das[9], Pieter Leyssen[10], Johan Neyts[10], Winston Chiu[10], Courtney A. Cohen[11], Jens Bukh[3,4,5], Judith Gottwein[3,4,5], John M. Dye[11], Norma Neff[12], Peter K. Jackson[7], Benjamin A. Pinsky[1,6], Tuomo Laitinen[13], Tatu Pantsar[13], Antti Poso[13], Fabio Zanini[14,15,16], Steven De Jonghe[10], Christopher R. M. Asquith[13] & Shirit Einav[1,12,17] ✉

In search for broad-spectrum antivirals, we discover a small molecule inhibitor, RMC-113, that potently suppresses the replication of multiple RNA viruses including SARS-CoV-2 in human lung organoids. We demonstrate selective inhibition of the lipid kinases PIP4K2C and PIKfyve by RMC-113 and target engagement by its clickable analog. Lipidomics analysis reveals alteration of SARS-CoV-2-induced phosphoinositide signature by RMC-113 and links its antiviral effect with functional PIP4K2C and PIKfyve inhibition. We identify PIP4K2C's roles in SARS-CoV-2 entry, RNA replication, and assembly/egress, validating it as a druggable antiviral target. Integrating proteomics, single-cell transcriptomics, and functional assays, reveals that PIP4K2C binds SARS-CoV-2 nonstructural protein 6 and regulates virus-induced autophagic flux impairment. Promoting viral protein degradation by reversing autophagic flux impairment is a mechanism of antiviral action of RMC-113. These findings reveal virus-induced autophagy regulation via PIP4K2C, an understudied kinase, and propose dual PIP4K2C and PIKfyve inhibition as a candidate strategy to combat emerging viruses.

Emerging viral infections pose major threats to human health. Severe acute respiratory syndrome coronavirus 2 (SARS-CoV-2) has resulted in over six million deaths. The incidence of mosquito-borne viral infections, such as those caused by the flavivirus dengue (DENV) and the alphavirus Venezuelan equine encephalitis virus (VEEV), has been increasing, in part due to global warming[1]. The filoviruses Ebola (EBOV) and Marburg (MARV), causative agents of lethal hemorrhagic fever, continue to cause outbreaks. No effective countermeasures are currently available for the majority of these and other emerging viral infections. The current prevailing strategy—targeting viral factors by direct-acting antivirals (DAAs)—is typically limited by a narrow-spectrum coverage and the emergence of drug resistance. There is thus a large unmet need for novel approaches, to be used individually or with DAAs. Targeting cellular kinases exploited by multiple viruses is one attractive approach to overcome these challenges and provide readiness for future outbreaks[2].

The phosphoinositide family consists of the membrane lipid phosphatidylinositol (PI) and its seven phosphorylation products, whose activity is tightly regulated by cellular kinases[3]. PI-3,5-bisphosphate [PI(3,5)P_2] is generated through 5′-phosphorylation of PI-3-monophosphate [PI(3)P] by PIKfyve (PI-3-phosphate 5-kinase) on late endosomal/lysosomal and autophagic compartments[4]. PIKfyve

A full list of affiliations appears at the end of the paper. ✉e-mail: seinav@stanford.edu

inhibition depletes PI(3,5)P_2, disrupting lysosomal function and causing lysosomal enlargement[5]. However, this effect is non-cytotoxic, as shown by the favorable safety profile of apilimod in clinical trials for inflammatory diseases[6]. PIKfyve is required for viral infections, and its pharmacological inhibition suppresses viral entry (coronaviruses, filoviruses) and/or egress (filoviruses, Lassa virus)[7,8].

PI-4,5-bisphosphate [PI(4,5)P_2] is formed via 4'-phosphorylation of PI5P by three PI-5-phosphate 4-kinases: products of the *PIP4K2A*, *PIP4K2B*, and *PIP4K2C* genes[9]. These isoforms, with significant structure similarity, differ in enzymatic activity and subcellular distribution[10]. Whereas PIP4K2A/B positively regulate autophagic flux, PIP4K2C knockdown reduces levels of autophagy cargo proteins and mutant huntingtin protein (mHTT), and positively regulates mTORC1[10–12]. Yet, PIP4K2C's biology is poorly understood, its role in viral infections is unexplored, and its therapeutic relevance remains unknown.

Various viruses impair autophagic flux to support their replication[13–15]. SARS-CoV-2 nonstructural 6 protein (NSP6) was shown to bind a subunit of the vacuolar ATPase, disrupting lysosomal acidification[16]. However, impaired autophagic flux is not currently targeted as an antiviral strategy.

While optimizing inhibitors of the NUMB-associated kinase GAK as an antiviral strategy[17], we identified a novel small molecule inhibitor, RMC-113, that did not suppress GAK activity. Here we discover that RMC-113 selectively inhibits PIP4K2C and PIKfyve and suppresses the replication of multiple RNA viruses. We probe the roles of these kinases in SARS-CoV-2 infection and the therapeutic potential and mechanism of antiviral action of RMC-113. Our findings validate PIP4K2C as a druggable antiviral target, beyond PIKfyve, demonstrating its binding to NSP6 and regulation at various stages of the SARS-CoV-2 life cycle, in part by controlling viral-induced autophagic flux impairment, thereby suppressing viral protein degradation. Moreover, our findings identify PIP4K2C and PIKfyve as the molecular targets of RMC-113, with enhanced autophagic flux as its antiviral mechanism, proposing a candidate for broad-spectrum antiviral development.

Results

RMC-113 demonstrates broad-spectrum antiviral activity in vitro and in human adult lung organoid (ALO)-derived monolayers, with a high genetic barrier to resistance

Structure-affinity relationship analysis of isothiazolo[4,3-*b*]pyridine-based analogs for targeting GAK[17] generated a 3,6-disubstituted analog, RMC-113, which exhibited low affinity to GAK (K_d=7.6 μM) (Fig. 1a). To determine the antiviral potential of RMC-113, we studied its effect against SARS-CoV-2. Five-day treatment with RMC-113 dose-dependently rescued Vero E6 cells constitutively expressing enhanced green fluorescent protein (eGFP) from SARS-CoV-2-induced lethality (isolate: Belgium-GHB-03021) (Fig. 1b–d). Similarly, RMC-113 dose-dependently inhibited replication of wild-type (WT) SARS-CoV-2 expressing Nluc-reporter (rSARS-CoV-2/Nluc (USA-WA1/2020 strain)) in human lung epithelial (Calu-3) cells, as measured via plaque (EC_{50} = 0.13 μM) and luciferase (EC_{50} = 1.45 μM) assays (Fig. 1e and Supplementary Fig. 1a). RMC-113 also suppressed replication-restricted pseudovirus bearing SARS-CoV-2 spike (S) protein (rVSV-SARS-CoV-2-S) in Vero cells (EC_{50} = 1.8 μM) (Supplementary Fig. 1b). No apparent effect on cellular viability was measured at the concentrations used in infected and uninfected cells via alamarBlue and CellTiter-Glo assays (CC_{50} > 20 μM, CC_{90} > 20 μM) (Fig. 1e and Supplementary Fig. 1a–c). Beyond SARS-CoV-2, RMC-113 dose-dependently inhibited the replication of the vaccine strain of VEEV (TC-83) in human astrocytes (U-87 MG) via luciferase assays (EC_{50} = 1.4 μM), DENV2 (EC_{50} = 1.4 μM) in human hepatoma (Huh7) cells via plaque assays, and EBOV (EC_{50} = 5 μM) and MARV (EC_{50} = 7.8 μM) in Huh7 cells via microneutralization assays, without apparent cellular toxicity (Supplementary Fig. 1d–g).

To assess the barrier to resistance, SARS-CoV-2 was passaged in TMPRSS2 expressing Vero E6 (Vero E6-TMPRSS2) cells in the presence of RMC-113 at concentrations ranging between the EC_{50} and EC_{90} values or DMSO, and infectious viral titers were measured in culture supernatants by plaque assays (Fig. 1f). No phenotypic resistance was observed over nine passages (Fig. 1g). Furthermore, SARS-CoV-2 harvested following nine passages under RMC-113 treatment remained susceptible to RMC-113 (Fig. 1h).

Next, we studied the effect of RMC-113 on SARS-CoV-2 infection in human adult stem cell-derived lung organoid (ALO)-monolayers composed of airway and alveolar cells[18,19] (Fig. 1i). RMC-113 dose-dependently suppressed SARS-CoV-2 replication measured in ALO culture supernatants by plaque assays (EC_{50} = 0.15 μM) and nucleocapsid (N) transcript expression measured in ALO lysates by RT-qPCR (EC_{50} = 0.35 μM), with CC_{90} > 10 μM (Fig. 1j, k). Moreover, RMC-113 treatment nearly abolished SARS-CoV-2 nucleocapsid (N) expression, as shown by confocal immunofluorescence (IF) analysis (Fig. 1l).

The observed activity of RMC-113 against several unrelated viruses highlights its broad-spectrum potential, while its high resistance barrier suggests it more likely targets cellular rather than viral functions.

RMC-113 selectively inhibits PIP4K2C and PIKfyve

To identify the putative cellular targets, we first conducted kinome profiling in cell lysates treated with RMC-113 via multiplexed inhibitor beads kinome profiling coupled with mass spectrometry (MIB/MS) on 224 kinases[20]. RMC-113 exhibited dose-dependent binding to PIKfyve, PIP4K2A, PIP4K2B, and PIP4K2C, with low or no binding to other kinases (Fig. 2a and Supplementary Fig. 2a). An orthogonal radiometric kinase activity screening of 335-kinases, excluding PIKfyve and PIP4K2s, measured no confirmed activity against any kinase, with an excellent selectivity score (S(50) = 0.003) at both 100 nM and 1 μM (Supplementary Data 1). RMC-113 potently bound recombinant PIKfyve (K_d=370 nM) and PIP4K2C (K_d=46 nM) and suppressed the enzymatic activity of PIKfyve (IC_{50} = 8 nM) (Fig. 2b–d). While no in vitro enzymatic assay currently exists for PIP4K2C, cell-based target engagement analysis via live-cell NanoBRET assays[21] revealed comparable activities on PIP4K2C and PIKfyve (IC_{50} = 392 nM and IC_{50} = 300 nM, respectively). No kinase activity (IC_{50} > 10 μM) and lower affinity (K_d=1.7 μM) were, however, measured on PIP4K2A and PIP4K2B, respectively (Fig. 2d).

To validate these targets, we designed a clickable analog, SRN2-002, by adding a terminal alkynyl motif with an aziridine photoaffinity group attached via an ethylene glycol linker, replacing the solvent-exposed 3,4-dimethoxyphenyl moiety[22] (Fig. 2e). SRN2-002 exhibited potent activity on PIKfyve (in vitro: IC_{50} = 6.35 nM; cell-based: IC_{50} = 462 nM) and moderate activity on PIP4K2C (in vitro: K_d = 610 nM; cell-based: IC_{50} = 3210 nM) (Fig. 2d). SRN2-002 dose-dependently suppressed SARS-CoV-2 infection in Calu-3 cells (EC_{50} = 0.23 μM, CC_{50} > 20 μM), comparably to RMC-113 (Fig. 2f). We confirmed the copper-catalyzed azide-alkyne cycloaddition CuAAC/click reaction between SRN2-002's alkyne and azide-biotin (Supplementary Fig. 2b,c). Although kinome profiling via MIB/MS SRN2-002 exhibited dose-dependent loss in binding to PIKfyve but not to PIP4K2C (Supplementary Fig. 3a), induced fit docking suggested plausible binding of SRN2-002 to the ATP-binding site of both kinases (Supplementary Fig. 3b,c) and that its reduced PIP4K2C activity may result from the tighter environment with the solvent-oriented clickable group. The approximately 13-fold difference in K_d values and 10-fold difference in cellular IC_{50} values between the parent compound (RMC-113) and the functionalized compound (SRN2-002) on PIP4K2C is likely driven in part by the removal of the meta-methoxy group (present in RMC-113 but not in SRN2-002).

To assess target engagement, SARS-CoV-2-infected A549-ACE2 cells were treated with SRN2-002 individually or along with (non-clickable) RMC-113, followed by UV irradiation of cell lysates to bind the click probe to targets, click reaction, pull-down with streptavidin beads,

https://doi.org/10.1038/s41467-025-61759-1

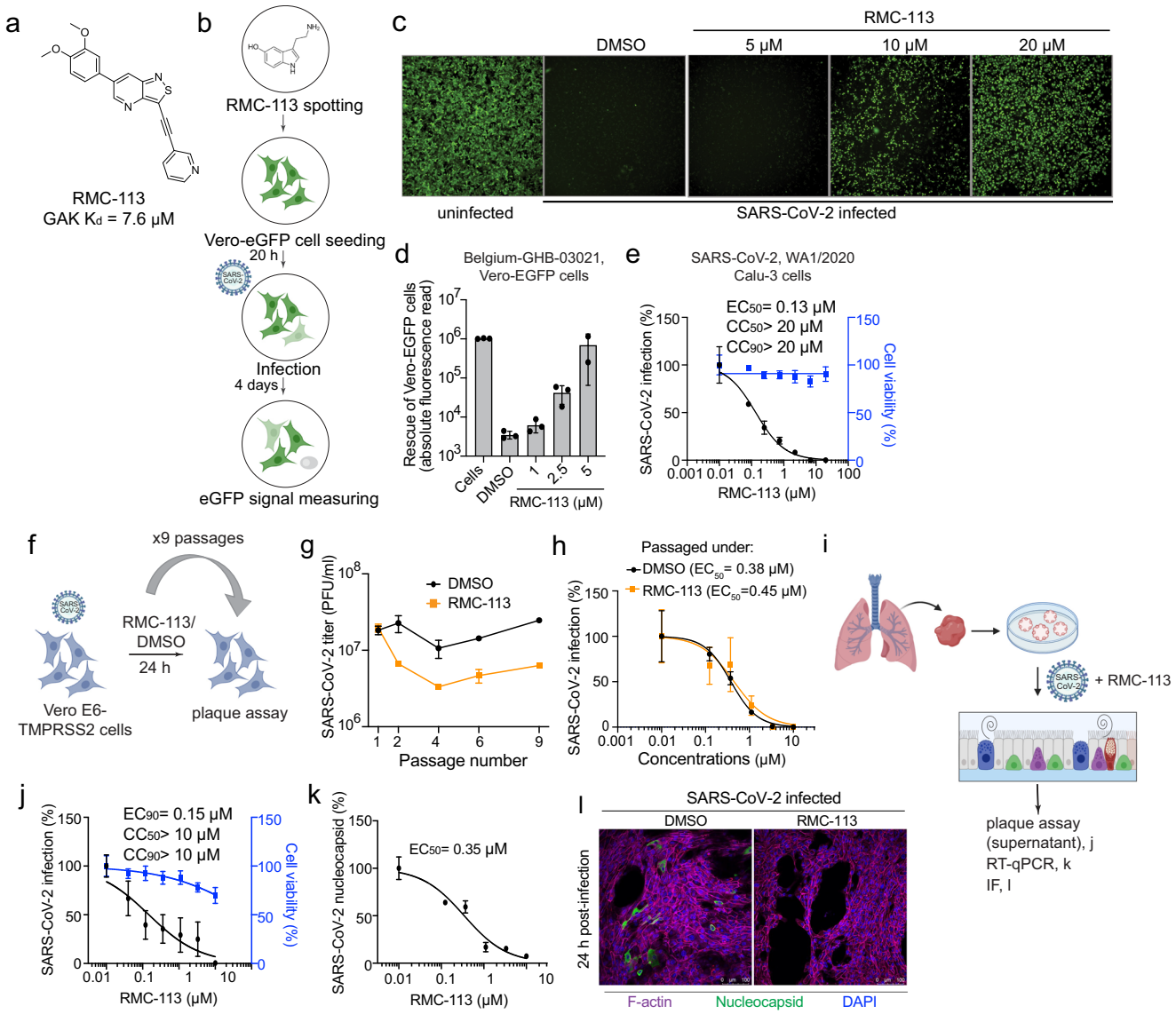

Fig. 1 | RMC-113 inhibits SARS-CoV-2 infection in vitro and in human ALOs with a high genetic barrier to resistance. a Chemical structure of RMC-113. **b** Rescue assay for virus-induced cell lethality. RMC-113 (10 μM) was incubated with Vero E6-eGFP cells for 20 h followed by SARS-CoV-2 infection. eGFP signal measured at 96 hpi indicates cell survival. **c** and **d** Fluorescence images (**c**) and corresponding graph (**d**) of Vero-eGFP cells rescued from SARS-CoV-2-induced lethality by RMC-113 (Belgium-GHB-03021 strain, MOI = 0.05). Original magnification, ×5 (c). e and j, Dose response to RMC-113 of SARS-CoV-2 infection [black, USA-WA1/2020 strain, MOI = 0.05 (**e**), 1 (**j**)] and cell viability (blue) in Calu-3 cells (**e**) or ALO-derived monolayer supernatants (**j**) via plaque and alamarBlue assays at 24 (**e**) or 48 (**j**) hpi, respectively. f and i, Schematics of the experiments shown in g (**f**) and j, k, l (**i**), respectively. Figure was created in BioRender. Karim, M. (2025) https://biorender.com/2yx5sx9. g, Vero E6-TMPRSS2 cells were infected with rSARS-CoV-2-nLuc virus (MOI = 0.05) and passaged daily under RMC-113 (0.1–0.3 μM) or DMSO over nine passages. Viral titers were measured by plaque assays. h, Dose response to RMC-113 of rSARS-CoV-2-nLuc virus harvested after nine passages under RMC-113 or DMSO via luciferase assays. **k** Dose response to RMC-113 of SARS-CoV-2 (MOI = 1) nucleocapsid copy number in ALO lysates measured by RT-qPCR assays at 48 hpi. **l** Confocal IF microscopy images of F-actin (violet), nucleocapsid (green), and DAPI (blue) in uninfected and SARS-CoV-2–infected ALOs, pretreated with DMSO or RMC-113 (5 μM) at 24 hpi. Representative merged images at x40 magnification are shown. Scale bars: 50 μm. Data shown are representative of independent experiments (**c**, **d**, **j**, **l**) or represent combined results from two ($n = 2$; **e**, **g**, **h**) or three ($n = 3$; k) independent experiments. Data in **e**, **h**, **j**, and **k** are relative to DMSO. Means ± SD are shown. Source data are provided as a Source Data file.

and immunoblotting. SRN2-002 (5 μM) pulled down PIKfyve and PIP4K2C, with minimal signal in non-UV irradiated samples. Addition of RMC-113 dose-dependently reduced PIKfyve and PIP4K2C pull-down, indicating effective competition and target engagement (Fig. 2g).

Collectively, these findings provide evidence that RMC-113 is a cell-active dual inhibitor of PIP4K2C and PIKfyve.

RMC-113 displays comparable binding at the active site of PIP4K2C and PIKfyve

To disclose the putative binding mode of RMC-113 to these kinases, we utilized molecular dynamics (MD) simulations[23]. Our microsecond timescale simulations suggest stable binding to RMC-113 with both PIKfyve and PIP4K2C in the ATP-binding site (Fig. 2h). Both kinases showed comparable binding modes with RMC-113, maintaining a constant hydrogen-bond with the hinge region throughout the simulations (PIP4K2C: Met206; PIKfyve: Leu1940) (Fig. 2h–l). Two phenylalanine residues located above and below the solvent-exposed region accommodate the aromatic dimethoxyphenyl in the binding pocket (PIP4K2C: Phe141, Phe207; PIKfyve: Phe1866, Phe1941). On the pyridyl-end of the molecule, π−π stacking is observed with an aromatic residue (PIP4K2C: Phe185; PIKfyve: Tyr2037). A key difference in the interactions of the solvent-exposed region between the kinases is the stable

https://doi.org/10.1038/s41467-025-61759-1

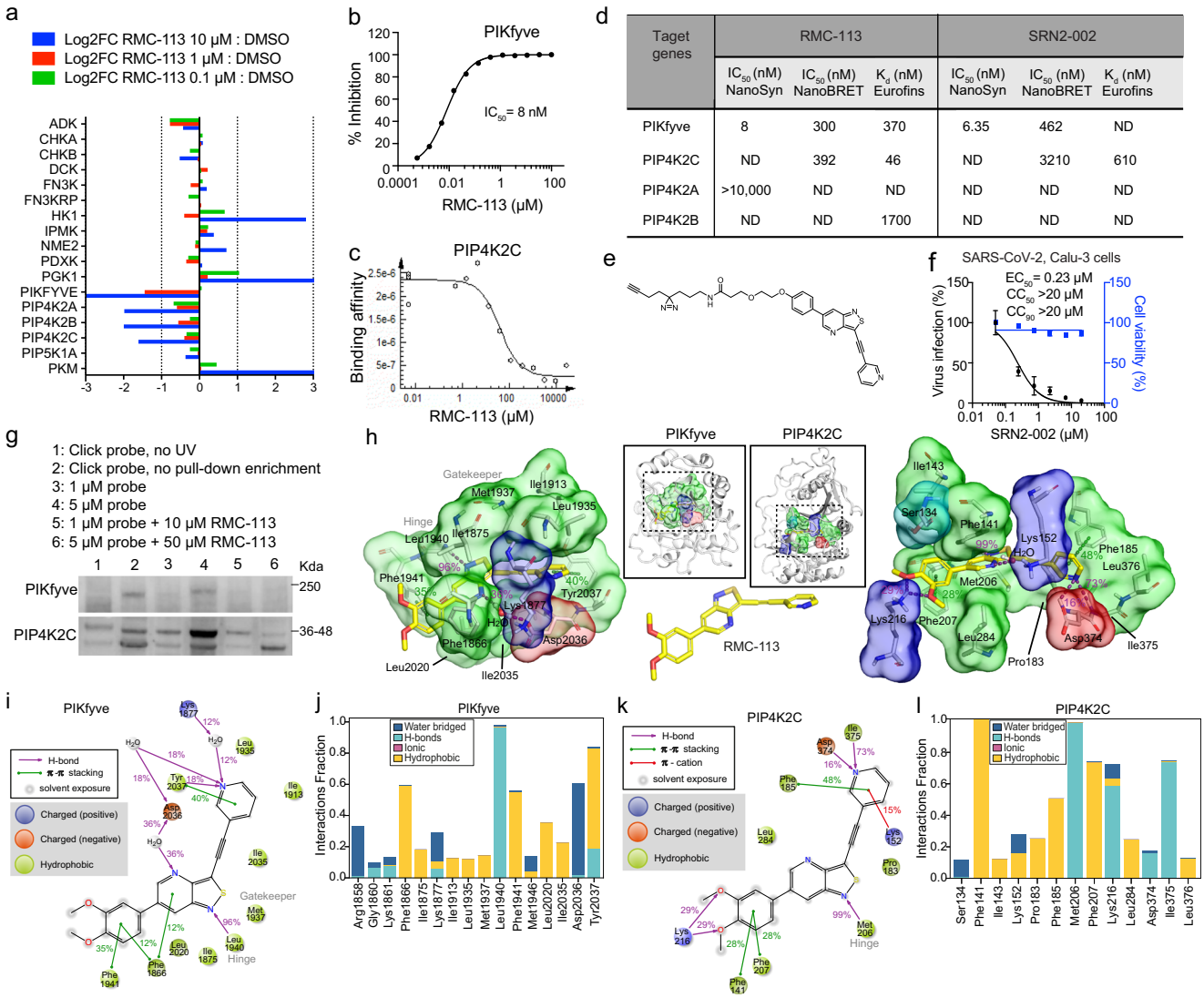

Taget genes	RMC-113			SRN2-002		
	IC_{50} (nM) NanoSyn	IC_{50} (nM) NanoBRET	K_d (nM) Eurofins	IC_{50} (nM) NanoSyn	IC_{50} (nM) NanoBRET	K_d (nM) Eurofins
PIKfyve	8	300	370	6.35	462	ND
PIP4K2C	ND	392	46	ND	3210	610
PIP4K2A	>10,000	ND	ND	ND	ND	ND
PIP4K2B	ND	ND	1700	ND	ND	ND

Fig. 2 | RMC-113 is a selective kinase inhibitor that stably binds PIKfyve and PIP4K2C. a Kinase abundance ratio between RMC-113 (0.1, 1.0, and 10 μM)- and DMSO-treated SUM159 cell lysates measured by multiplexed inhibitor beads kinome profiling and mass spectrometry (MIB/MS). Shown are the Log2 fold change mean values ± SD of 2 replicates of a subset of the screen panel (see Supplementary Fig. 2a). **b** and **c** In vitro dose response of PIKfyve activity (**b**) and PIP4K2C binding (**c**) to RMC-113. **d** Biochemical parameters for RMC-113 and SRN2-002. ND = Not determined. **e** Chemical structure of SRN2-002. **f** Dose response of SARS-CoV-2 infection (MOI = 0.05, black) and cell viability (blue) to SRN2-002 in Calu-3 cells via plaque and alamarBlue assays at 24 hpi, respectively ($n = 2$ independent experiments). **g** Kinase expression in SARS-CoV-2-infected A549-ACE2 lysates following incubation with SRN2-002 individually or combined with RMC-113, UV irradiation, and streptavidin pull-down measured by Western blotting at 24 hpi. Representative membranes of $n = 2$ experiments are shown. Lanes: 1: SRN2-002, no UV; 2: SRN2-002, no pull-down; 3: SRN2-002 (1 μM); 4: SRN2-002 (5 μM); 5: SRN2-002 (1 μM) competitively inhibited by RMC-113 (10 μM); 6: SRN2-002 (5 μM) competitively inhibited by RMC-113 (50 μM). h, Putative binding mode of RMC-113 into the kinase ATP-binding pockets based on microsecond timescale MD simulations. A representative snapshot with key interactions is shown (see i–l for details). Binding pocket residues with >10% interaction frequencies to RMC-113 are shown. Positively charged residues are highlighted in blue; negative charge, red; hydrophobic, green; polar, cyan. RMC-113 is shown in yellow (carbon) stick model. H-bonds are illustrated with purple dashed lines, π–π interactions with green. i and k, Summary of main protein-ligand interactions (> 10% frequency) in the MD simulations of PIKfyve (**i**) and PIP4K2C (**k**). **j** and **l** Aggregate of protein-ligand interactions (residues with >10%) in the simulations of PIKfyve (**j**) and PIP4K2C (**l**). Means ± SD are shown (**f**). Data in (**i** and **j**) consist of 72 μs, and (k and l) consist of 20 μs, both analyzed each 1 ns. Source data are provided as a Source Data file.

interaction with Lys216 observed in PIP4K2C, but not in PIKfyve. RMC-113 behaves similarly in complex with these kinases, with the one key movement within the binding being an occasional flip with the solvent-exposed dimethoxyphenyl-groups (Fig. 2i, j and Supplementary Fig. 4a, b). The pyridyl-end of the molecule appears slightly more stable with PIP4K2C, likely due to the direct hydrogen-bond interactions via its nitrogen (Fig. 2k, l and Supplementary Fig. 4a, b). Notably, both kinase domains display high flexibility in the simulations, highlighting their specific characteristics (Supplementary Fig. 4b–d).

Overall, these simulations imply stable binding of RMC-113 to both kinases, consistent with the experimental data.

PIKfyve and PIP4K2C are required for effective SARS-CoV-2 infection and are the molecular targets mediating the antiviral effect of RMC-113

To define the molecular targets mediating RMC-113's antiviral effect, we assessed the effect of siRNAs targeting PIKfyve and PIP4K2C in SARS-CoV-2-infected Calu-3 cells via plaque assays. Knockdown efficiency was confirmed via RT-qPCR and immunoblotting (Fig. 3a–c), and no cytotoxicity was observed (Fig. 3d and Supplementary Fig. 5a). Depletion of PIKfyve and PIP4K2C suppressed SARS-CoV-2 replication by over 2 logs relative to a non-targeting (siNT) control (Fig. 3d).

https://doi.org/10.1038/s41467-025-61759-1

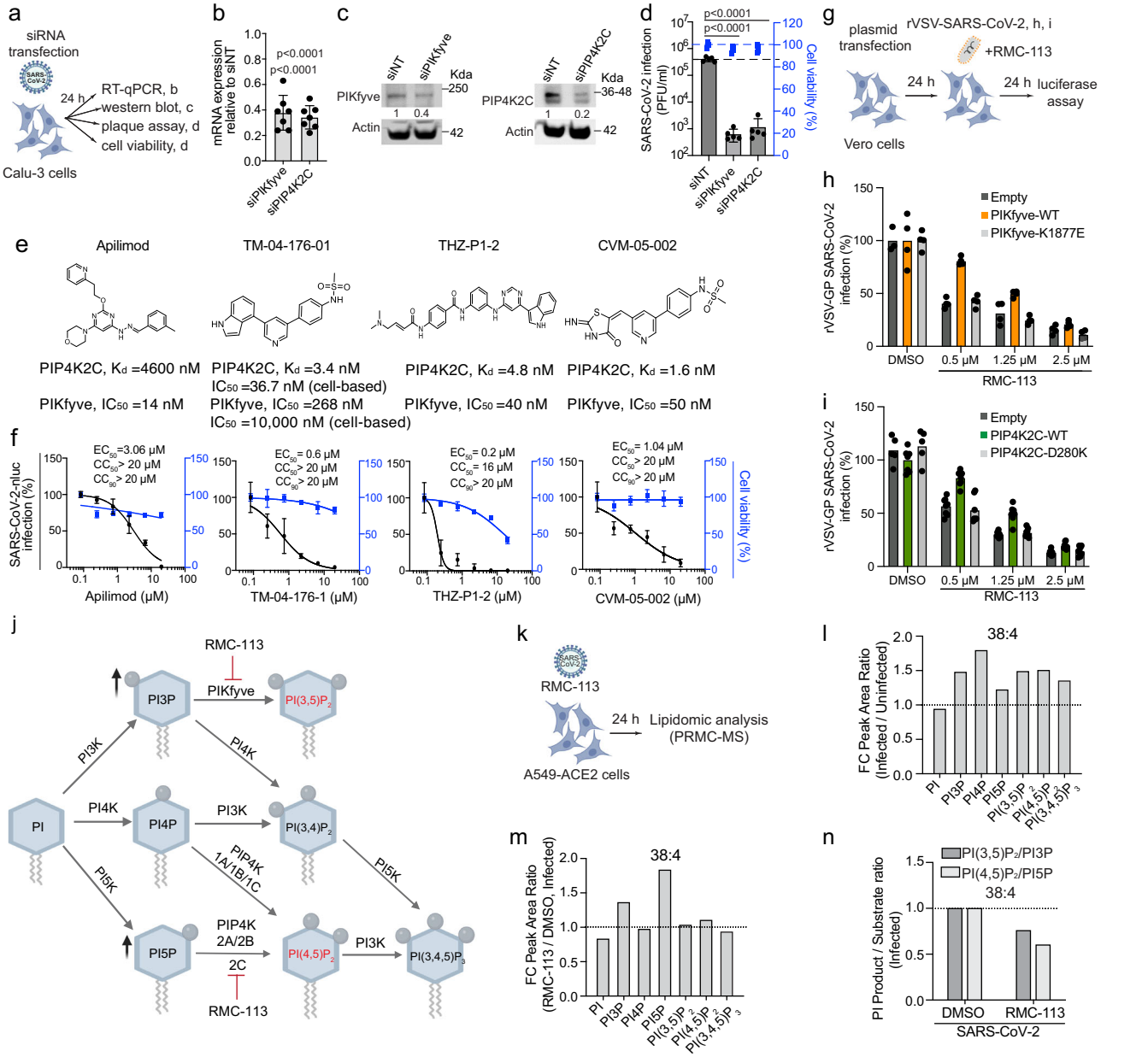

Fig. 3 | PIKfyve and PIP4K2C are essential for SARS-CoV-2 infection and mediate the antiviral effect of RMC-113. a, **g**, **k**, Schematics of the experiments in **b**, **c**, **d** (**a**); **h**, **i** (g); and **l**, **m**, **n** (k). **b** and **c** Confirmation of siRNA-mediated knockdown of PIKfyve and PIP4K2C by RT-qPCR (**b**) and Western blot (**c**) in Calu-3 cells. Shown are gene expression levels normalized to GAPDH relative to respective gene levels in siNT control (**b**) and representative membranes and quantitative data (**c**) at 48 h post-transfection. **d** Viral titers (PFU/ml) and cell viability (blue) in Calu-3 cells transfected with the indicated siRNAs at 24 hpi with SARS-CoV-2 (MOI = 0.05) via plaque and alamarBlue assays, respectively. **e** Chemical structures of PIKfyve and/or PIP4K2C inhibitors. **f** Dose response of rSARS-CoV-2-nLuc (black, USA-WA1/2020 strain, MOI = 0.05) infection and cell viability (blue) in Calu-3 cells via luciferase and alamarBlue assays at 24 hpi, respectively. **h** and **i** Rescue of rVSV-SARSCoV-2-S infection under RMC-113 treatment upon ectopic expression of WT PIKfyve (**h**) and PIP4K2C (**i**) their kinase-dead mutants or empty control plasmids measured by luciferase assays at 24 hpi in Vero cells. **j** Schematic representation of phosphoinositides and associated kinases. Figure was created in BioRender. Karim, M. (2025) https://biorender.com/yynkvs0. l and m, Fold change (FC) of peak area ratio of the indicated phosphoinositides in SARS-CoV-2-infected (MOI = 0.5) vs. uninfected (l) and RMC-113- vs. DMSO-treated infected A549-ACE2 cells (**m**) as measured via PRMC-MS. n, Product-to-substrate ratios in RMC-113- vs. DMSO-treated cells infected with SARS-CoV-2 (**l**, **m**). Data shown are representative of independent experiments (**c**) or represent combined results from two ($n = 2$; f, h, i) or three ($n = 3$; b, d) independent experiments. Data is relative to siNT (**b**, **d**) or DMSO (**f**, **h**, **i**). Means ± SD are shown (**b**, **d**, **f**, **h**, **i**). **l**, **m**, **n** represent one of two independent experiments. See an associated experiment in Supplementary Fig. 6e–g and Supplementary Data 2. P values by 1-way ANOVA followed by Dunnett's (**b**, **d**) multiple-comparison test are indicated. Source data are provided as a Source Data file.

We assessed the requirement of these kinases by testing the anti-SARS-CoV-2 effects of chemically distinct investigational compounds targeting PIKfyve and/or PIP4K2C (Fig. 3e). Apilimod, a selective PIKfyve inhibitor (in vitro: $IC_{50} = 14$ nM)[4], dose-dependently inhibited the replication of SARS-CoV-2 both in Calu-3 cells ($EC_{50} = 3.06$ μM, $CC_{50} > 20$ μM), as reported[7], and ALOs ($EC_{50} = 0.42$ μM, $CC_{50} > 10$ μM) (Fig. 3f and Supplementary Fig. 5b-d). TM-04-176-01, a selective PIP4K2C inhibitor (K_d=3.4 nM; cell-based PIP4K2C: $IC_{50} = 36.7$ nM, PIKfyve: $IC_{50} = 10{,}000$ nM)[24], potently suppressed SARS-CoV-2 replication ($EC_{50} = 0.6$ μM, $CC_{50} > 20$ μM) (Fig. 3f). THZ-P1-2 and CVM-05-002, inhibitors of PIKfyve and PIP4K2C[24,25], also inhibited SARS-CoV-2 infection

(EC_{50} = 0.2 μM and EC_{50} = 1.04 μM, respectively), albeit THZ-P1-2 demonstrated greater cytotoxicity (CC_{50} = 16 μM) (Fig. 3f).

To verify that RMC-113's antiviral mechanism is mediated, at least in part, by inhibition of the kinase activity of PIKfyve and PIP4K2C, we conducted "rescue" experiments in Vero cells infected with rVSV-SARS-CoV-2-S. Ectopic expression of WT, but not catalytically inactive PIKfyve (K1877E) and PIP4K2C (D280K) mutants or a control plasmid, completely or partially reversed the effect of RMC-113 on viral entry (Fig. 3g–i and Supplementary Fig. 5e–h).

A549-ACE2 cells expressing 2xFYVE, mCherry-fused PI3P marker, showed cytosolic vacuolation and swelling of membrane structures, positive for endosomal markers (EEA-1, Rab-7), upon RMC-113 and apilimod treatment (Supplementary Fig. 5i–k), supporting PIKfyve suppression without alteration of its subcellular distribution.

Unlike PIKfyve[7], the functional relevance of PIP4K2C in viral infections has not been previously demonstrated. These findings provide genetic and pharmacological validation that PIP4K2C, beyond PIKfyve, is a druggable antiviral target and a molecular target mediating the effect of RMC-113 on viral entry.

RMC-113 alters the phosphoinositide regioisomer signature by advanced lipidomics analysis

To determine the impact of RMC-113 treatment on phosphoinositide abundance, lipid extracts derived from uninfected and SARS-CoV-2-infected A549-ACE2 cells were subject to lipidomic analysis. Employing phosphoinositide regioisomer measurement by chiral column chromatography and mass spectrometry (PRMC-MS)[26], we comprehensively profiled all eight PI classes and their acyl chain variants (defined by carbon number and saturation level) (Fig. 3j, k). Seven phosphoinositide classes (except for $PI(3,4)P_2$) were detected in all tested conditions. Upon SARS-CoV-2 infection, the abundance of multiple PI classes was increased relative to uninfected samples, albeit with some variability across independent experiments (Fig. 3l and Supplementary Fig. 6a). This increase was most pronounced with the abundant acyl chain (38:4) (Fig. 3l), yet a similar trend was observed with other acyl chains (Supplementary Fig. 6b-e and Supplementary Data 2). Notably, RMC-113 treatment in infected cells caused a 1.5-2-fold increase in the abundance of PI3P and PI5P—the substrates of PIKfyve and PIP4K2C, respectively (Fig. 3j)—relative to DMSO (Fig. 3m and Supplementary Fig. 6f). Whereas the respective phosphorylated products, $PI(3,5)P_2$ and $PI(4,5)P_2$, were unaltered (likely due to intact activity of enzymes not targeted by RMC-113, such as PIP4K (1 A/1B/1 C)), the product-to-substrate ratios of PIKfyve and PIP4K2C were reduced in both uninfected and infected cells upon RMC-113 treatment relative to DMSO (Fig. 3j, m, n and Supplementary Fig. 6g). Similar results were observed with other acyl chain variants (Supplementary Data 2).

These findings provide evidence that the antiviral effect of RMC-113 is correlated with functional inhibition of PIP4K2C and PIKfyve activities and propose modulation of virus-induced PI signature as a candidate mechanism of antiviral action.

PIP4K2C is required for SARS-CoV-2 entry, RNA replication and assembly/egress, whereas PIKfyve is required for viral entry only

To pinpoint the steps of the viral life cycle impacted by RMC-113, we conducted time-of-addition experiments. RMC-113 was added to Calu-3 cells upon infection or at 2, 5, or 8 hpi with SARS-CoV-2 (Fig. 4a). Cell culture supernatants were harvested at 10 hpi (corresponding to a single viral replication cycle in Calu-3 cells), and infectious viral titers were measured by plaque assays. RMC-113 treatment initiated upon infection onset and maintained throughout the 10 h experiment (0–10) suppressed viral infection by 99.5% relative to DMSO (Fig. 4b). RMC-113 treatment during the initial 2 h of infection (0–2) suppressed viral infection by 79.4%, confirming an effect on entry of WT SARS-CoV-2 (beyond rVSV-SARS-CoV-2-S) (Fig. 4b and Supplementary Fig. 1b). Following extensive washing at 2 hpi (to remove the viral inoculum), addition of RMC-113 at 2, 5, and 8 hpi suppressed viral infection by 97, 96, and 69.3%, respectively, indicating inhibition at post-entry stages (Fig. 4b). In contrast, apilimod suppressed SARS-CoV-2 replication when added during the first two hpi, but not at later time points (Fig. 4c).

RMC-113 dose-dependently suppressed intracellular SARS-CoV-2 N copy number (EC_{50} = 0.137 μM) at 2 hpi of Calu-3 cells with a high-inoculum virus relative to DMSO, as measured by RT-qPCR, validating an effect on SARS-CoV-2 entry (Fig. 4d, e). Moreover, RMC-113 dose-dependently inhibited the replication of in vitro transcribed RNA encoding a nano-luciferase reporter-based SARS-CoV-2 subgenomic replicon deleted for three structural proteins[27] in Vero E6 cells. Similar to ensitrelvir, albeit with a higher EC_{50} value (1.5 vs. 0.06 μM), this effect reveals that RMC-113 also suppresses viral RNA replication (Fig. 4f, g). In contrast, apilimod suppressed rVSV-SARS-CoV-2-S pseudovirus infection (Fig. 4h, i), confirming its effect on SARS-CoV-2 entry, yet it dose-dependently increased viral RNA replication (Fig. 4j). RMC-113 treatment initiated at a post-entry stage did not alter the intracellular expression pattern of non-structural protein 6 (NSP6), its colocalization with the ER morphogenic protein RTN3—two markers of double-membrane vesicles (DMV) biogenesis[28]—and the number of NSP6-RTN3 colocalized puncta per cell relative to DMSO controls (Supplementary Fig. 7a, b).

To probe the requirement for PIKfyve and PIP4K2C in viral entry and RNA replication, we conducted the assays described above in cells depleted for the individual lipid kinases by siRNAs (Fig. 4d, f). Depletion of PIKfyve and PIP4K2C suppressed SARS-CoV-2 entry by 81.7 and 73.8%, respectively, relative to siNT as measured at 2 hpi by RT-qPCR (Fig. 4d, k). Moreover, depletion of PIP4K2C, but not PIKfyve, suppressed replication of the subgenomic replicon (Fig. 4f, l).

These findings pinpoint the role of PIKfyve specifically in SARS-CoV-2 entry and the role of PIP4K2C in viral entry, RNA replication, and assembly/egress. Concordantly, RMC-113, but not apilimod, suppresses temporally distinct stages of the SARS-CoV-2 life cycle.

RMC-113 reverses SARS-CoV-2-induced impairment of autophagic flux and promotes viral protein degradation

To test the hypothesis that by suppressing PIP4K2C RMC-113 modulates autophagy, we studied its effect on autophagosome formation and autophagic flux first via IF analysis of multiple single A549-ACE2 cells expressing the premo-GFP-RFP-LC3 reporter and stained for SARS-CoV-2 N protein (Fig. 5a). Since GFP fluorescence is quenched in the acidic lysosomes whereas RFP signal is stable, in this assay, autophagosomes appear as yellow (RFP+/GFP+) and autolysosomes as red (RFP+/GFP-) puncta (Fig. 5b and Supplementary Fig. 7c). Upon SARS-CoV-2 infection, we measured a 2.4-fold increase in the number of yellow puncta and a 1.2-fold decrease in the number of red puncta relative to uninfected controls (Fig. 5c and Supplementary Fig. 7d). The autophagic flux (autolysosome-to-autophagosome or red-to-yellow puncta ratio) was 2.4 times lower in infected vs. uninfected cells (Fig. 5c,d). Concurrently, the expression signals of p62 (autophagy cargo) and LC3-II (mature autophagosome marker) were greater in SARS-CoV-2-infected vs. uninfected (DMSO-treated) A549-ACE2 cells, as measured via immunoblotting (Fig. 5e). These results provide evidence that SARS-CoV-2 impairs autophagic flux, in agreement with prior studies[16,29]. While ULK1 expression (an autophagy initiation marker) was unchanged upon SARS-CoV-2 infection (Supplementary Fig. 7e), prior studies reported variable effects of SARS-CoV-2 on autophagy initiation, suggesting a dynamic regulation[29,30].

RMC-113 treatment caused a 2-fold reduction in the number of yellow puncta in SARS-CoV-2-infected cells, over a 5-fold increase in the number of red puncta, and 7.6-fold increase in the autolysosome-to-autophagosome ratio relative to DMSO in the IF analysis (Fig. 5c,d, Supplementary Fig. 7d), revealing induction of autophagic flux. Moreover, it caused a 2–5.2-fold and a 7.4–10.4-fold reduction in p62

https://doi.org/10.1038/s41467-025-61759-1

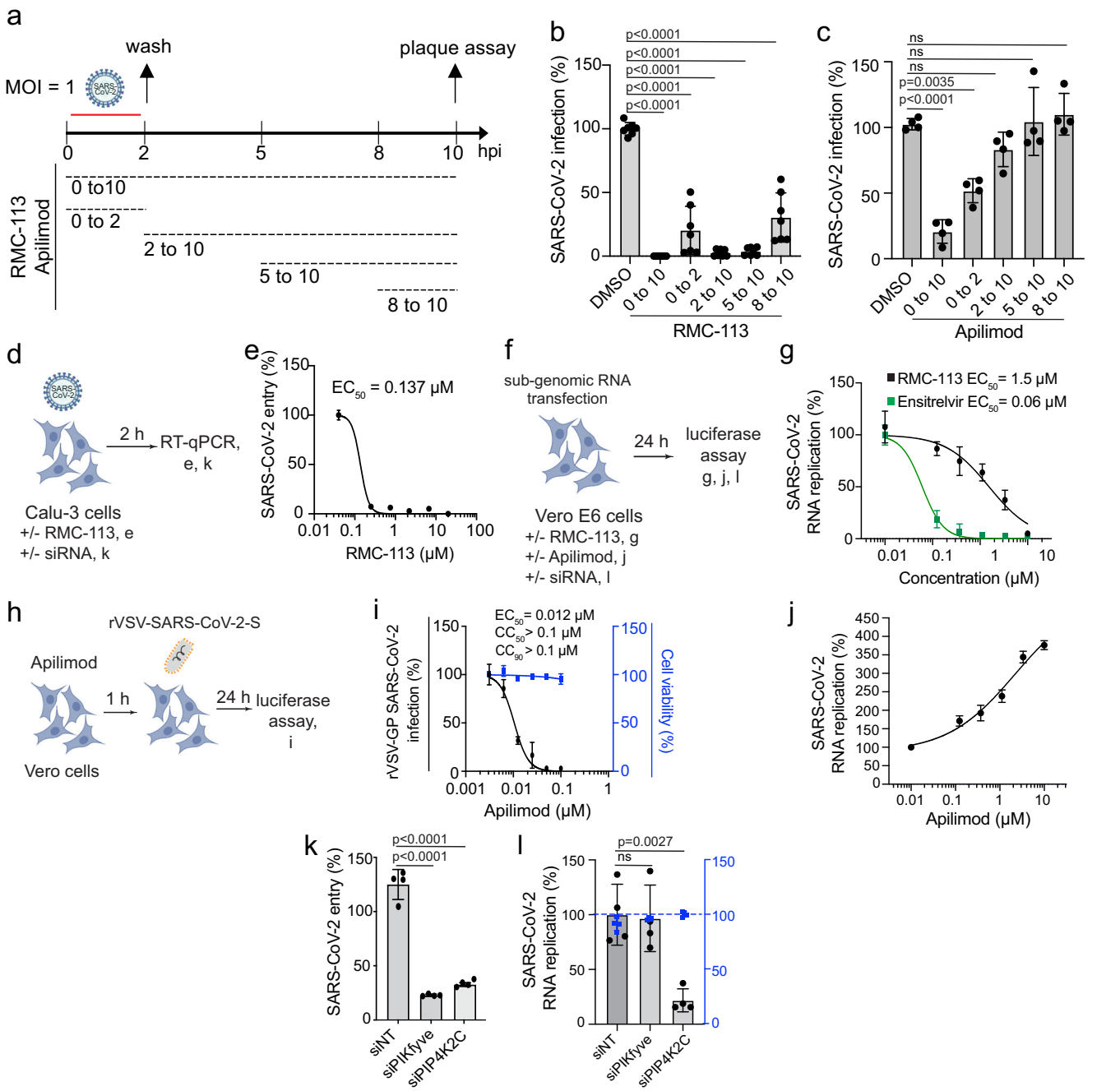

Fig. 4 | PIP4K2C is required for temporally distinct stages of the SARS-CoV-2 life cycle, whereas PIKfyve is required for viral entry only. a Schematic of the time-of-addition experiments shown in **b**, **c**. **b** and **c** Calu-3 cells were infected with WT SARS-CoV-2 (MOI = 1). At the indicated times, RMC-113 (10 µM) (**b**), apilimod (10 µM) (**c**), or DMSO were added. Supernatants were collected at 10 hpi, and viral titers measured by plaque assays. d, f and h, Schematics of the experiments shown in **e**, **k** (**d**); **g**, **j**, **l** (**f**) and **i** (**h**). **e**, Dose response to RMC-113 of WT SARS-CoV-2 entry (MOI = 1) in Calu-3 cell lysates measured by RT-qPCR assays at 2 hpi. g, Dose response to RMC-113 and ensitrelvir of viral RNA replication measured by luciferase assay in Vero E6 cells 24 h post-transfection of in vitro transcribed nano-luciferase reporter-based SARS-CoV-2 subgenomic non-infectious replicon[27]. **i** Dose response to apilimod of rVSV-SARS-CoV-2-S infection (black) and cell viability (blue) in Vero cells via luciferase and alamarBlue assays at 24 hpi, respectively. **j** Dose response to apilimod of viral RNA replication measured by luciferase assay in Vero E6-TMPRSS2 cells 24 h post-transfection of in vitro transcribed nano-luciferase reporter-based SARS-CoV-2 subgenomic non-infectious replicon[27]. **k** WT SARS-CoV-2 (MOI = 1) entry measured in Calu-3 cells depleted of the indicated kinases using corresponding siRNAs by RT-qPCR at 2 hpi. l, Viral RNA replication and cell viability (blue) measured by luciferase and alamarBlue assays, respectively, in Vero E6 cells depleted of the indicated kinases, 24 h post-transfection of in vitro transcribed nano-luciferase reporter-based SARS-CoV-2 subgenomic non-infectious replicon[27]. Data shown are representative of independent experiments (**i**) or represent combined results from two ($n = 2$; **e**, **g**, **j**) or three ($n = 3$; **b**, **c**, **k**, **l**) independent experiments. Means ± SD are shown. Data is relative to DMSO (**b**, **c**, **e**, **g**, **i**, **j**) or siNT (**k**, l). P values by 1-way ANOVA followed by Tukey's (**b**, **c**) or Dunnett's (**k**, **l**) multiple-comparison test are indicated. ns= non-significant. Source data are provided as a Source Data file.

and LC3-II expression signals, respectively, in uninfected and SARS-CoV-2-infected A549-ACE2 and VeroE6-TMPRSS2 cells, relative to DMSO (Fig. 5e-g and Supplementary Fig. 7f-i), consistent with enhanced autophagic degradation. In contrast, apilimod and chloroquine (CQ), an inhibitor of autophagosome-lysosome fusion[31], moderately reduced the autolysosome number and the autolysosome-to-autophagosome ratio relative to DMSO (Fig. 5c, d and Supplementary Fig. 7d). Moreover, the colocalization of LC3 with LAMP-1

https://doi.org/10.1038/s41467-025-61759-1

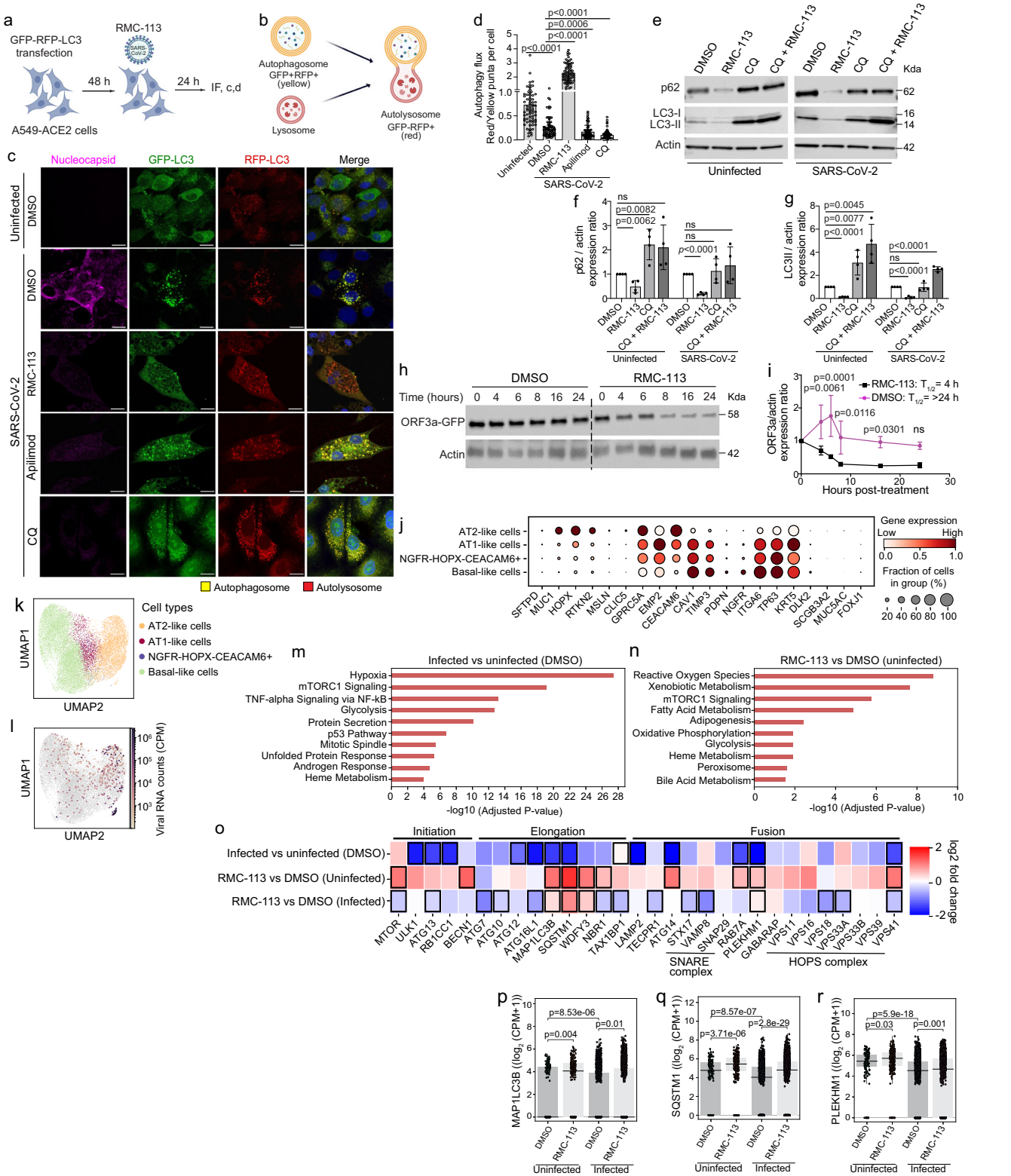

(lysosomal marker) was greater in GFP-RFP-LC3-expressing cells upon treatment with RMC-113 than apilimod and CQ, suggesting increased autophagosome-lysosome fusion by this compound (Supplementary Fig. 7j).

Next, we sought to determine whether the observed reduction in yellow puncta and LC3-II upon RMC-113 treatment resulted solely from increased autophagic flux or also from reduced autophagosome formation and maturation. ULK1 expression levels were comparable in RMC-113- and DMSO-treated cells (Supplementary Fig. 7e). Moreover, no reduction in autophagosome maturation was observed under conditions where autophagic degradation was blocked: in fact, there was a 2.5-fold increase in LC3-II signal upon addition of RMC-113 two hours post-treatment with a saturating concentration (10 μM) of CQ[32] compared to DMSO in SARS-CoV-2-infected cells (Fig. 5e and Supplementary Fig. 7g). Comparable trends were observed, albeit with a greater magnitude, when CQ was added for 4 (vs. 24) hours prior to cell lysis (Fig. 5e and Supplementary Fig. 7f, g). These findings favor increased autophagy flux over reduced autophagosome formation by RMC-113.

Fig. 5 | RMC-113 reverses SARS-CoV-2-induced impairment of autophagic flux and accelerates viral protein degradation. a Schematic for **c** and **d**. **b** Autophagy flux: from autophagosomes (yellow, RFP + /GFP +) to autolysosomes (red, RFP +/GFP-). Figure was created in BioRender. Karim, M. (2025) https://biorender.com/yynkvs0. c, Representative confocal images (x40) of A549-ACE2 cells expressing GFP-RFP-LC3, infected with SARS-CoV-2 (MOI = 0.5), treated with DMSO, RMC-113 (5 μM), apilimod (5 μM) or CQ (10 μM) for 24 h, and stained for nucleocapsid (violet). Scale bars: 10 μm. Zoomed-in images: autophagosomes (yellow); autolysosomes (red). d, Autolysosome-to-autophagosome ratio in 70 single cells (**c**). **e**–**g** Autophagy marker expression in uninfected and SARS-CoV-2-infected (MOI = 1) A549-ACE2 lysates treated with RMC-113 (5 μM) and/or CQ (10 μM) or DMSO at 24 hpi via immunoblotting (**e**). Quantification of p62/actin (**f**) and LC3II/actin (**g**) ratios normalized to DMSO ($n = 4$ membranes). h and i, Representative membranes (**h**) and quantification (**i**) ($n = 3$ membranes) showing ORF3A half-life in A549-ACE2 lysates after RMC-113 (5 μM) or DMSO treatment. j, Marker genes annotating cell populations. Color: expression (cpm); dot size: expressing cell fraction. **k** and **l** UMAP embedding of scRNA-seq dataset indicating distinct cell types (**k**) or SARS-CoV-2 transcripts (**l**). **m** and **n** Pathway enrichment in AT2 cells infected vs. uninfected (**m**) and RMC-113 vs. DMSO treated (**n**) ALOs. **o**, Heatmap of log2 fold-change in autophagy-related genes between infected vs. uninfected (DMSO), RMC-113 vs. DMSO (uninfected), and RMC-113 vs. DMSO (infected) AT2-like cells at 24 hpi. Black rectangles: significant changes (Wilcoxon test). See Supplementary Fig. 8b. **p**–**r** Box plots of gene expression in individual AT2 cells at 24 hpi. Horizontal lines indicate quartiles; whiskers extend to ±1.5 × interquartile range. Adjusted *P* values (two-sided Wilcoxon test, Benjamini-Hochberg correction). Data are representative of independent experiments (**c**, **e**, **h**) or combined results from three ($n = 3$; **d**, **i**–**r**) or four ($n = 4$; **f**, **g**) independent experiments. Means ± SD are shown (**d**, **f**, **g**, **i**). P values by 1-way (**d**) or 2-way (**i**) ANOVA with Tukey's (**d**) or two-tailed unpaired t-test (**f**, g) or Šídák's (**i**) multiple comparison test are indicated. ns= non-significant. Source data are provided as Source Data file.

To test the hypothesis that PIP4K2C-regulated impaired autophagic flux impacts degradation of SARS-CoV-2 proteins, we measured the effect of RMC-113 on the half-life of ORF3a and the non-structural protein 3 (NSP3). RMC-113 treatment reduced the half-life of ectopically expressed ORF3a from >24 to 4 h and of NSP3 from >8 to 4.4 h in A549-ACE2 cells relative to DMSO (Fig. 5h, i and Supplementary Fig. 7k, l). Since measured in uninfected cells, this time-dependent reduction in ORF3a and NSP3 expression did not result from an effect of RMC-113 on viral replication, but rather on protein degradation.

These findings provide evidence that RMC-113, but not apilimod, promotes autophagic degradation arrested by SARS-CoV-2 and this effect is mediated by PIP4K2C (vs. PIKfyve) inhibition. Moreover, they highlight reduced viral protein degradation as one mechanism by which PIP4K2C promotes SARS-CoV-2 replication.

Virus-inclusive scRNA-seq (viscRNA-seq) analysis reveals temporal SARS-CoV-2-induced autophagy signatures and partial reversion by RMC-113

To determine whether the observed induction of autophagic degradation by RMC-113 is accompanied by transcriptional regulation of autophagy and/or lysosomal functions, we characterized the transcriptional response to SARS-CoV-2 infection and RMC-113 treatment in correlation with viral RNA (vRNA) abundance via viscRNA-seq analysis[33]. Using PARSE technology in ALOs at 4 and 24 hpi and treatment, we recovered 20,672 high-quality cells (Supplementary Fig. 8a) and identified four major cell populations: alveolar epithelial type II (AT2)-like, AT1-like, and basal-like cells, as well as NGFR-HOPX-CEACAM6+ cells, likely representing various differentiation stages (Fig. 5j,k). AT2-like cells were the main viral RNA-harboring cells (VHCs) (Fig. 5l).

Gene ontology (GO) analysis of differentially expressed genes (DEGs) in AT2-like cells revealed mTORC1 signaling, implicated in autophagy regulation[10,12], among the top-upregulated pathways upon infection and RMC-113 treatment (Fig. 5m,n). We thus focused the differential expression analysis on genes involved in autophagy and lysosomal functions. At 4 hpi, AT2-like cells from SARS-CoV-2-infeced ALOs exhibited downregulation of *mTOR* along with upregulation of autophagy initiation genes (*ULK1, ATG13, RB1CC1, BECN1*) relative to uninfected ALOs, and variable regulation of genes involved in elongation and fusion, suggesting infection-induced autophagy initiation. While a variable pattern was observed in uninfected ALOs, RMC-113 treatment of SARS-CoV-2-infected ALOs was associated with upregulation of *mTOR* and elongation factors (e.g. *SQSTM1, MAP1LC3B*), downregulation of *BECN1*, and variable regulation of fusion genes relative to DMSO (Supplementary Fig. 8b).

At 24 hpi, AT2-like cells from SARS-CoV-2-infected ALOs demonstrated mild upregulation of *mTOR* along with profound downregulation of multiple genes involved in autophagy initiation (*ULK1, ATG13, RB1CC1*), elongation [*ATG12, ATG16L1, MAP1LC3B* (p62), *SQSTM1* (LC3-II), *TAX1BP1*] and fusion (*LAMP2, ATG14, RAB7A, PLEKHM1, VPS41*) relative to uninfected ALOs. In uninfected ALOs, RMC-113 treatment induced upregulation of genes involved in all stages of autophagy, particularly elongation (*MAP1LC3B, SQSTM1, WDFY3, NBR1*) and fusion [*ATG14, RAB7A, PLEKHM1* and member of the SNARE (*VAMP8*) and HOPS (*VPS41*) complexes] relative to DMSO (Fig. 5o). In SARS-CoV-2-infected ALOs, RMC-113 treatment resulted in a more variable signature with upregulation of some elongation (*MAP1LC3B, SQSTM1, WDFY3*) and fusion (*PLEKHM1, GRABARAP)* genes, yet downregulation of others, as the SNARE (*STX17, VAMP8*) and HOPS (*VPS18, VSP33A*, *VSP41*) complex genes, relative to DMSO (Fig. 5o). Several genes including *MAP1LC3B*, *SQSTM1*, *PLEKHM1, ATG14 and WDFY3* demonstrated a pattern wherein expression level was downregulated upon SARS-CoV-2 infection (vs. no infection) in DMSO-treated ALOs and upregulated in response to RMC-113 treatment (Fig. 5p-r, and Supplementary Fig. 8c,d). The overall expression levels of autophagy genes were slightly higher in VHCs than bystander cells in both DMSO and RMC-113-treated ALOs (Supplementary Fig. 8e,f).

Downregulation of multiple genes involved in lysosomal functions was observed at 24 hpi in infected vs uninfected ALOs. These included membrane transporters, hydrolyses, multiple subunits of the v-ATPase complex and genes involved in lysosomal biogenesis and other functions (Supplementary Fig. 9). In contrast, RMC-113 treatment induced upregulation of multiple genes in the same categories, including membrane transporters (e.g. *LAPTM4A, LMBRD1, LAMP1*); hydrolyses (e.g. *CTSZ, GGH, GNS*), and v-ATPase complex subunits (Supplementary Fig. 9).

These findings indicate a transcriptional effect of SARS-CoV-2 infection on autophagic and lysosomal genes and propose partial reversion of this phenotype as a potential mechanism of antiviral action of RMC-113.

PIP4K2C binds SARS-CoV-2 NSP6 and regulates SARS-CoV-2-induced impairment of autophagic flux

Repeating the functional autophagic flux experiments using a genetic approach revealed that siRNA-mediated PIP4K2C depletion caused a 41.6% reduction in the number of yellow puncta along with a 31.4% increase in the number of red puncta, and a 2.6-fold increase in the autolysosome-to-autophagosome ratio relative to siNT control via IF analysis of SARS-CoV-2- infected A549-ACE2 cells (Fig. 6a–c and Supplementary Fig. 10a, b). A similar pattern was observed in uninfected A549-ACE2 cells (Supplementary Fig. 10b, c). Concurrently, PIP4K2C depletion caused a 1.3–4.2-fold reduction in p62 and LC3-II expression signals relative to siNT control as measured by immunoblotting in both uninfected and SARS-CoV-2-infected A549-ACE2 cells (Fig. 6d-f).

In contrast, PIKfyve depletion did not significantly alter the autolysosome-to-autophagosome ratio via IF analysis (Fig. 6a–c and Supplementary Fig. 10a–c), yet it resulted in 2.1-6.6-fold increase in p62 and LC3-II expression signals relative to siNT in uninfected and SARS-

CoV-2-infected A549-ACE2 cells (Fig. 6g–i), in agreement with prior reports in uninfected cells[12,34]. Similar findings were observed with siPIP4K2C and siPIKfyve in VeroE6-TMPRSS2 cells (Supplementary Fig. 10d–j).

Lastly, to determine if PIP4K2C plays a direct role in SARS-CoV-2 infection, we screened for its interactions with 15 nonstructural SARS-CoV-2 proteins and two accessory proteins—ORF3a, ORF7a—shown to impair autophagosome-lysosome fusion in SARS-CoV-2 infected cells[15] – via protein-fragment complementation assays (PCAs). Plasmids encoding Gluc1-PIP4K2C and individual Gluc2-tagged viral proteins were transfected pairwise into HEK-293T cells followed by luciferase assays. A cutoff value of >2.2 SDs (corresponding to normalized luminescence ratio (NLR) > 10) relative to a random reference set composed of 15 noninteracting human protein pairs[35] was chosen as the threshold to define positive interactions. PIP4K2C bound NSP3 and NSP6, whereas its co-expression with other viral proteins yielded background-level signals (Fig. 6j). Additionally, confocal microscopy analysis demonstrated colocalization of endogenous PIP4K2C with overexpressed Flag-tagged NSP6 in A549-ACE2 cells, with a mean Manders' colocalization coefficient (M2: NSP6 overlapping PIP4K2C) of 0.56 (Fig. 6k,l).

We propose a model wherein PIP4K2C binds SARS-CoV-2 NSP6 and regulates impairment of autophagic flux by altering the phosphoinositide composition on autophagosomal and/or lysosomal membranes (Fig. 6m). By acting on additional membranes, PIP4K2C regulates temporally distinct viral life cycle stages. RMC-113 reverses PIP4K2C-suppressed viral protein autophagic degradation, beyond PIKfyve-mediated entry, thereby simultaneously targeting two key pathways implicated in SARS-CoV-2 and other viral infections.

Discussion

There is an urgent need for novel antivirals to combat emerging viral infections. Impaired autophagic flux, a conserved mechanism exploited by various viruses[13–15], is not currently targeted directly by pharmacological interventions (without inducing global autophagy). Integrating biochemical, virologic, pharmacological, genetic, single-cell transcriptomics, proteomics, and lipidomics approaches with functional assays, we uncover PIP4K2C as a key regulator of SARS-CoV-2 infection interacting with NSP6. We provide insight into the underlying mechanism: PIP4K2C regulates virus-induced autophagic flux impairment, suppressing viral protein degradation. Moreover, we reveal the therapeutic potential and mechanism of antiviral action of dual inhibition of PIP4K2C and PIKfyve as a novel broad-spectrum antiviral strategy.

We identified PIP4K2C, not previously implicated in viral infections, as a druggable antiviral target using a pharmacological probe, RMC-113. We validate the requirement for PIP4K2C in SARS-CoV-2 infection genetically and with a chemically distinct selective PIP4K2C inhibitor. Utilizing a panel of assays with WT SARS-CoV-2, pseudovirus and subgenomic replicon, we show that PIP4K2C regulates viral entry, RNA replication and an assembly/egress stage. Although not ubiquitously expressed in all cell types and organs, its regulation at temporally-distinct viral life cycle stages, likely facilitated by its presence on various membranes (plasma, autophagosomes, Golgi[10]), highlights that PIP4K2C acts as a key regulator of SARS-CoV-2 infection and an attractive candidate antiviral target.

The observed reduced p62 and LC3-II protein degradation and autolysosome-to-autophagosome ratio upon SARS-CoV-2 infection supports virus-induced autophagic flux impairment, as previously reported in coronaviral infections[15,29]. Nevertheless, the cellular mechanism that regulates this process remained unknown and untargeted. We provide pharmacological and genetic evidence that PIP4K2C is a key regulator of SARS-CoV-2-induced autophagic flux impairment. Prior demonstration of reduced autophagy cargo expression and mHTT aggregates upon PIP4K2C suppression indicate a role in autophagy[11,12], yet PIP4K2C is largely understudied, possibly due to its low abundance and only recent development of pharmacological tools[24,25]. Phenotypically, we show a partially reversed transcriptomic autophagy signature by viscRNA-seq upon RMC-113 treatment. Demonstrating reduced p62 and LC3-II protein expression, along with an increased autolysosome-to-autophagosome ratio in SARS-CoV-2-infected cells upon PIP4K2C suppression via siPIP4K2C or RMC-113 (but not siPIKfyve or apilimod) treatment in two cell lines, functionally validates PIP4K2C's role in autophagic flux impairment. Notably, we provide evidence that suppression of autophagic flux by PIP4K2C, preventing degradation of some viral proteins, is a mechanism by which PIP4K2C regulates SARS-CoV-2 replication.

The discovery that PIP4K2C binds NSP6 supports its direct role in SARS-CoV-2 infection and suggests that it may regulate NSP6-mediated functions, such as lysosomal deacidification via ATP6AP1 binding[16]. Probing PIP4K2C's role in regulation of NSP6 and other SARS-CoV-2 proteins shown to impair autophagosome-lysosome fusion (ORF3a, ORF7a, NSP15)[15] is a topic for future research. Moreover, although our IF analysis did not support the hypothesis that PIP4K2C regulates NSP6-induced DMV formation[28], additional work is necessary to definitively test this hypothesis.

Our findings point to RMC-113 as a candidate antiviral for further development. RMC-113 inhibits replication of RNA viruses from four families: corona-, flavi-, alpha- and filoviruses. Moreover, passaging SARS-CoV-2 under RMC-113 treatment does not select for escape mutations, albeit the interpretation of these data in the absence of DAA controls (avoided to prevent gain of function mutations) is somewhat limited.

We discovered that RMC-113 selectively inhibits PIP4K2C and PIKfyve using cutting-edge biochemical technologies, MD simulation and a clickable probe[12]. Moreover, we provide multiple lines of evidence that modulating PIP4K2C's and PIKfyve's enzymatic activities is an important antiviral mechanism of RMC-113. First, measuring increased levels of PI5P—PIP4K2C's substrate and a low-abundance, least-studied phosphoinositide[36], previously shown to induce autophagy[12]—and PI3P by comprehensive lipidomics profiling, links RMC-113's antiviral effect with suppression of PIP4K2C and PIKfyve and modulation of autophagic flux[12]. Second, RMC-113 mimics siPIP4K2C in suppressing SARS-CoV-2 entry, RNA replication, and infectious virus production, and in reversing the autophagic flux impairment. Third, WT PIKfyve and PIP4K2C, but not their kinase-dead mutants, reverse RMC-113's anti-SARS-CoV-2 effect.

Extending previous findings[29], the viscRNA-seq analysis on ALOs reveals temporal regulation, with upregulation of autophagy genes at SARS-CoV-2 entry followed by downregulation of autophagy and lysosomal genes at 24 hpi. Among the genes downregulated in SARS-CoV-2-infected relative to uninfected cells, yet upregulated by RMC-113 treatment, particularly in VHCs, are the elongation factors *MAP1LC3B* (LC3B) as well as *SQSTM1* and *WDFY3*, whose encoded proteins (p62 and ALFY) form a complex tethered to autophagosome membranes, recruiting ubiquitinated protein aggregates[37]. Contrastingly, p62 and LC3II protein levels increased following infection and decreased upon RMC-113 treatment. Thus, while suppression of autophagic flux at the protein level is a primary result of infection, cells might activate transcriptional downregulation to compensate for these virus-induced changes. Supporting this hypothesis, cells that controlled infection (zero vRNA counts) suppressed *SQSTM1* and *WDFY3* expression more than cells that failed to control infection (1+ viral counts).

The transcript levels of *PLEKHM1* (facilitates autophagosome-lysosome fusion by interacting with components of the HOPS and SNARE complexes[38]) and *GABARAP* (a ubiquitin-like modifier on autophagosomes to which PLEKHM1 binds) were also downregulated in infected ALOs and upregulated upon RMC-113 treatment, yet with no correlation with vRNA presence. It is tempting to speculate that by reversing the autophagic flux impairment, RMC-113 promotes binding

https://doi.org/10.1038/s41467-025-61759-1

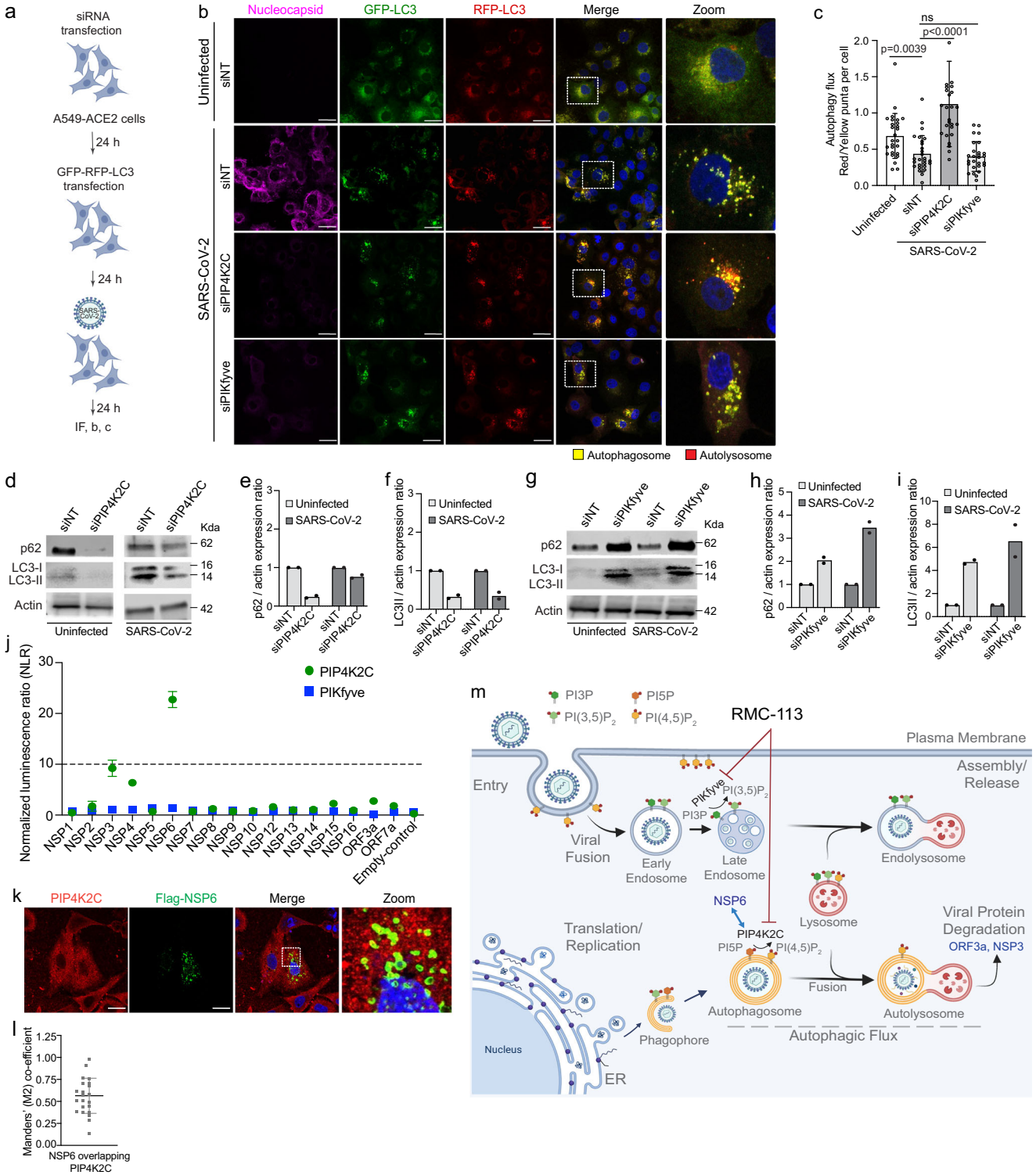

of ubiquitinated viral proteins, such as NSP6 and the nucleocapsid[39,40], to these cargo receptors and their degradation. The observed upregulation of genes involved in lysosomal functions upon RMC-113 treatment offers additional exploratory paths.

Our findings suggest that simultaneous inhibition of PIP4K2C and PIKfyve by RMC-113 may provide better protection over PIKfyve-only inhibitors. Our results exclude a role for PIKfyve in post-entry stages, extending prior findings that PIKfyve mediates SARS-CoV-2 entry[7]. Moreover, while suppressing its role in endosomal functions is protective[7], we and others provide evidence that PIKfyve inhibition mildly suppresses autophagic flux[12,34], which could reduce the antiviral effect. These findings may explain why siPIKfyve and apilimod had no effect or even increased viral RNA replication, respectively, in our replicon data, and why apilimod and two other PIKfyve inhibitors could not achieve viral clearance and protection from SARS-CoV-2 infection in mice[41]. The suboptimal pharmacokinetic profile of apilimod has also limited its clinical development[42], yet its excellent safety profile in human clinical trials for inflammatory diseases, has de-risked PIKfyve as a target[6]. While our data in ALOs are promising, the in vivo safety and activity of PIP4K2C suppression remains to be determined. Developing dual PIP4K2C/PIKfyve inhibitors may benefit conditions beyond viral infections, including Huntington's disease and cancer[11,12,43].

Fig. 6 | PIP4K2C binds SARS-CoV-2 NSP6 and mediates virus-induced impairment of autophagic flux. a Schematic of the experiment shown in **b** and **c**. **b** Representative confocal microscopic images of A549-ACE2 cells transfected with indicated siRNAs and GFP-RFP-LC3 tandem plasmid, and infected with SARS-CoV-2 (MOI = 0.5) for 24 h and stained for nucleocapsid (violet). Representative merged images at x40 magnification are shown. Scale bars: 10 µm. Zoomed-in images show autophagosomes (yellow) and autolysosomes (red). **c** Autolysosome-to-autophagosomes ratio (autophagy flux) in single cells ($n = 27$ cells per category) (**b**). **d**–**i** The expression levels of p62, LC3-I and LC3-II following transfection of siPIP4K2C (**d**–**f**) and siPIKfyve (**g**–**i**) in uninfected and SARS-CoV-2-infected A549-ACE2 cell lysates at 24 hpi. Bar graphs show quantitative analysis of p62/actin (**e**, **h**) and LC3II/actin ratios (**f**, **i**), from 2 membranes and normalized to corresponding siNT controls. **j** PIP4K2C and PIKfyve interactions with 15 SARS-CoV-2 nonstructural proteins, ORF3a, ORF7a, and empty plasmid as measured via protein-fragment complementation assay (PCAs) in HEK293T cells. Dots depict mean NLR values. The dotted line depicts the cutoff (NLR > 10) used to define PIP4K2C-interacting proteins (green), representing greater than two SDs above the mean NLR of a non-interacting reference set. **k** and **l** Confocal IF microscopy images of PIP4K2C (red) and NSP6 (green) in A549-ACE2 cells ectopically expressing FLAG-NSP6 24 h after transfection. Shown are images at 60× magnification with a 6-fold zoom in (right panel) (**k**) and Manders' colocalization coefficients (M2: NSP6 overlapping PIP4K2C) (**l**) in 32 cells. Scale bar: 10 µm. **m** Proposed model for the roles of PIP4K2C and PIKfyve in SARS-CoV-2 infection and the mechanism of antiviral action of RMC-113. Figure was created in BioRender. Karim, M. (2025) https://biorender.com/glw3z17. Data are representative of independent experiments (**b**, **d**, **g**, **k**) or combined from two ($n = 2$; **e**, **f**, **h**, **i**, **j**) or three ($n = 3$; **c**, **l**) independent experiments. Data are relative to siNT (**c**, **e**, **f**, **h**, **i**). Means ± SD are shown (**c**, **l**). P values by 1-way ANOVA followed by Dunnett's multiple comparison test are shown (**c**). Source data are provided as a Source Data file.

In summary, our study identifies PIP4K2C, an understudied kinase, as a proviral factor required for SARS-CoV-2-mediated autophagic impairment and validates it as a druggable antiviral target. We propose dual inhibition of PIP4K2C and PIKfyve as a candidate therapeutic strategy for further development to enhance preparedness for viral outbreaks.

Methods

Study approval

SARS-CoV-2 and filovirus work were conducted in BSL3 and BSL4 facilities at Stanford University, KU Leuven Rega Institute, and USAMRIID according to CDC and institutional guidelines. Human lung organoid (ALO) propagation was approved under protocol IRB 190105 at UCSD.

Compounds

RMC-113 (Steven De Jonghe)[17], Apilimod (Selleckchem, S6414), Rapamycin (Med chem express, #HY-10219), Bafilomycin A1 (Invivogen, #tlrl-baf1), Chloroquine diphosphate (Premo Autophagy Tandem Sensor RFP-GFP-LC3B Kit, Thermo Scientific, # P36239). THZ-P1-2, CVM-05-002 and TM-04-176-01[24] were a gift from Dr. Nathanael S. Gray, Stanford University.

Plasmids

Plasmids used to produce SARS-CoV-2 pseudovirus were a gift from Jing Lin (Vitalant, San Francisco)[44]. The rSARS-CoV-2/WT and rSARS-CoV-2/Nluc (rSARS-CoV-2 expressing Nluc-reporter gene) plasmids were a gift from Dr. Luis Martinez-Sobrido. DENV2 (New Guinea C strain) TSV01 Renilla reporter plasmid (pACYC NGC FL) was a gift from Dr. Pei-Yong Shi (University of Texas Medical Branch)[45]. mCherry-2xFYVE plasmid was obtained from Addgene (#140050). SARS-CoV-2 subgenomic ΔS-E-M replicon was provided by Drs. Judith Gottwein and Jens Bukh (Copenhagen University Hospital, Denmark). VEEV-TC-83-nLuc RNA (a gift from Dr. William Klimstra (Department of Immunology, University of Pittsburgh, Pittsburgh). GFP-hPIKfyve (Addgene, #121148) cloned in gateway entry plasmid pDON221 and pDONR223-PIP4K2C (Addgene, #23450). Open reading frames encoding viral proteins were recombined into a gateway-compatible pGluc fusion expressing vectors using Gateway technology (Invitrogen). Mutations were introduced by site-directed mutagenesis using the QuikChange Lightning Site-Directed Mutagenesis Kit (Agilent).

Cells

Vero E6 cell line engineered to constitutively express enhanced green fluorescent protein (eGFP) was provided by Dr. Marnix Van Loock (Janssen Pharmaceutica, Beerse, Belgium) and was maintained in Dulbecco's modified Eagle's medium (DMEM, Gibco) supplemented with 10% v/v fetal calf serum (FCS, Biowest), 0.075% sodium bicarbonate and 1% penicillin-streptomycin (Pen-strep, Gibco). Vero E6, Vero, Caluu-3, HEK-293T, U-87 MG, and BHK-21 cells (ATCC, CRL-1586, CCL-81, HTB-55, CRL-3216, HTB-14, CCL-10) and Huh7 cells (Apath LLC) were maintained in DMEM supplemented with 10% fetal bovine serum (FBS, Omega Scientific, Inc), 1% L-glutamine, 1% Pen-strep, 1% nonessential amino acids (NEAA, Gibco), 1% HEPES (Gibco), 1% Sodium pyruvate (Thermo Fisher Scientific). Vero E6-TMPRSS2 (JCRB cell bank, #JCRB1819) and A549-ACE2 cells (BEI resources, NR-53821) were maintained in DMEM supplemented with 10% FBS, 1% Pen-strep, and 1 mg/ml G418 (Gibco, #10131035). All cells were maintained in a humidified incubator with 5% CO_2 at 37 °C and tested negative for mycoplasma by MycoAlert (Lonza, Morristown, NJ).

Human adult lung organoids (ALOs) model

The ALO model was generated from adult stem cells isolated from deep lung biopsy specimens. This model consists of cell types found in both proximal and distal airway epithelia, as validated previously[18]. Lung-organoid-derived monolayers were prepared as outlined[18,19] and plated in Pneumacult Ex-Plus Medium (StemCell Technologies).

Cell viability assays

Cell viability was assessed using alamarBlue reagent (Invitrogen) or CellTiter-Glo (Promega) according to the manufacturer's protocol. Fluorescence or luminescence were detected using GloMax Discover Microplate Reader (Promega).

Viral stocks preparation and sequencing

The Belgium-GHB-03021 strain of SARS-CoV-2 was isolated from a nasopharyngeal swab obtained from a patient returning from China in early February 2020[46] and passaged 6 times on Vero E6 cells. Viral stocks for rSARS-CoV-2/WT and rSARS-CoV-2/Nluc were generated as previously described[19]. Viruses produced in Vero E6-TMPRSS2 cells and passaged 3-4 times were used for the experiments. SARS-CoV-2 whole-genome sequencing was performed as previously described[19], and showed no deletions in the spike multi-basic cleavage (MBC) domain. VEEV-TC-83-nLuc RNA was transcribed in vitro from cDNA plasmid templates linearized with MluI via MEGAscript SP6 kit (Invitrogen #AM1330) and electroporated into BHK-21 cells. DENV RNA was transcribed in vitro from pACYC-DENV2-NGC plasmid using mMessage/mMachine kits (Ambion) and electroporated into BHK-21 cells. EBOV (Kikwit isolate) and MARV (Ci67 strain) (BEI Resources) were grown in Vero E6 cells. Supernatants were collected, clarified, and stored at −80 °C, and viral titers were determined via plaque assays on BHK-21 (DENV, VEEV) or Vero E6 cells (SARS-CoV-2, EBOV, MARV).

For rVSV-SARS-CoV-2-S pseudovirus production, HEK-293T cells were transfected with spike expression plasmid followed by infection with VSV-G pseudotyped ΔG-luciferase VSV virus and harvesting of culture supernatant, as described[19]. rVSV-SARS-CoV-2-S was titrated via luciferase assay, and $TCID_{50}$ was determined on Vero cells.

Infection assays and pharmacological inhibition

Unless otherwise specified, inhibitors or DMSO were added 1–2 h (cells) and 4 h (ALOs) prior to viral inoculation and maintained throughout the experiment. Calu-3, Vero cells, or ALOs were infected with SARS-CoV-2 (MOI = 0.05 or 1) in DMEM containing 2% FCS or 1X PneumaCult™-Ex Plus Medium at 37 °C under biosafety level 3 (BSL3) conditions. Following a 1 to 4-hour incubation, the viral inoculum was removed, and cells were washed thoroughly and supplemented with fresh medium. At various time points postinfection, culture supernatants were collected for measurement of viral titer using standard plaque assays[47], and cells were lysed in TrizolLS for RT-qPCR analysis. Huh7 cells were infected with DENV2 in (MOI = 0.05) and at 48 hpi, viral replication was measured via luciferase assays. Huh7 cells were infected with EBOV (MOI = 1) or MARV (MOI = 2) under BSL4 conditions. At 48 hpi, cells were formalin-fixed for 24 h prior to removal from BSL4 facility. Infected cells were detected using specific monoclonal antibodies against EBOV (KZ52) or MARV (7E6) glycoproteins and quantitated by automated fluorescence microscopy using an Operetta High Content Imaging System (PerkinElmer).

Antibodies

Immunoblotting. Antibodies targeting PIKfyve (Thermo Scientific, #PA5-75977), PIP4K2C (Sigma, #WH0079637M1, Sigma), SQSTM1/p62, (Cell Signaling Technology, #5114), LC3A/B (D3U4C) XP® Rabbit mAb (Cell Signaling Technology, #12741), and β-actin (Sigma-Aldrich, #A3854), ULK1 (D8H5) Rabbit mAb (Abcam, #8054), Gaussia luciferase Polyclonal Antibody (Thermo Scientific, #PA1-181), PIKFYVE Polyclonal Antibody (Thermo Scientific, #PA5-13977), Flag (DYKDDDDK) Tag Polyclonal Antibody (Thermo Scientific, #PA1-984B).

Immunofluorescence. Antibodies targeting SARS-CoV-2 nucleocapsid (SinoBiological, #40143-MM05), EEA-1 (Abcam, #ab109110), anti-LAMP1 (Abcam, #ab24170), Rab7 (Origene, #AB0033-200) RTN3 Monoclonal Antibody (Thermo Scientific, #1E11 MA5-15538), NSP-6 Anti-SARS-CoV-2 antibody (Abcam, #EPR24845-90). Goat anti-Mouse IgG (H + L), cross-absorbed secondary antibody, Alexa Fluor™ 633 (Thermo Scientific # A-21052A-21050), Goat anti-rabbit IgG (H + L), cross-absorbed secondary antibody, Alexa Fluor™ 488 (Thermo Scientific #A-11008).

RNA interference

ON-TARGETPlus siRNA against PIKfyve, PIP4K2C, and SMARTpools non-targeting siRNA (siNT) (D-001206-13-05), were purchased from Dharmacon/ Horizon Discovery. siRNA sequences: PIKfyve—GGAAA UCUCCUGCUCGAAAUU; PIP4K2C—CCGAGUCAGUUGGACAACGAUU.

siRNA transfection

siRNAs (10 pmol/well) were transfected into Calu-3, Vero E6, VeroE6-TMPRSS2 or A549-ACE2 cells using Dharmafect-4 (Dharmacon, #T-2004-02), lipofectamine RNAiMAX (Invitrogen) or Polyplus-transfection INTERFERin® (Genesee Scientific, #55-129), respectively, 48 h prior to viral infection.

Rescue assays

Plasmids encoding PIKfyve, PIP4K2C, or controls, were transfected into Vero cells using Lipofectamine 3000 reagent (Invitrogen) 24 h before treatment and viral infection. Viral infection and cell viability were measured 24 hpi via luciferase and alamarBlue assays, respectively.

RT-qPCR assays

The cells were lysed with TRIzolLS (Invitrogen). The total RNA was extracted from cell lysates using Direct-zol RNA Miniprep Plus Kit (Zymo Research) and reverse-transcribed using High-Capacity cDNA RT kit (Applied Biosystems), following the manufacturer's instructions. Primers and PowerUp SYBR Green Master Mix (Applied Biosystems) were added to the samples, and PCR reactions were performed with QuantStudio3 (Applied Biosystems). Target genes were normalized to GAPDH. Sequences of primers used for RT-qPCR are available upon request.

Time-of-addition experiment

Calu-3 cells were infected with SARS-CoV-2 (MOI = 1). Following 2 hpi for SARS-CoV-2, the virus inoculum was removed, and cells were washed twice with PBS. At specific time intervals, 10 µM RMC-113 or apilimod and 0.1% DMSO were added. Cell culture supernatants were collected at 10 hpi (SARS-CoV-2), and infectious viral titers were measured by plaque assays.

Resistance studies

Vero E6-TMPRSS2 cells were infected with SARS-CoV-2 (MOI = 0.05) and passaged daily 9 times by transferring an equal volume of viral supernatant to naive cells under DMSO or RMC-113 treatment at concentrations between the EC_{50} and EC_{90} values: 0.1 µM, passage 1; 0.3 µM passages 2–9. Viral titers in culture supernatants were measured by plaque assays.

SARS-CoV-2 entry assay

Calu-3 cells were infected with SARS-CoV-2 (MOI = 1). At 2 hpi, the viral inoculum was removed, and cells were washed three times with PBS. Cells were then lysed in TRIzolLS (Invitrogen), and intracellular viral RNA levels were measured by RT-qPCR.

SARS-CoV-2 subgenomic replicon assay

The ΔS-E-M Nluc replicon was generated as described in[27]. Briefly, full-length DNA was linearized with NotI, followed by purification with the Zymo DNA clean & concentrator-25 kit but using Zymo-Spin™ IC-XL columns (ZR BAC DNA Miniprep Kit, ZymoResearch, Irvine, CA, USA). The linearized plasmid was in vitro transcribed using the mMESSAGE mMACHINE T7 Transcription Kit (ThermoFisher, Waltham, MA, USA) following the manufacturer's instructions. RNA transcripts were quantified using the Qubit RNA BR Assay Kit (ThermoFisher, Waltham, MA, USA) and used for transfection. To measure RNA replication, in vitro transcribed replicon RNA was transfected into Vero E6 cells using Lipofectamine® MessengerMAX (#LMRNA015), 24 h prior to treatment with RMC-113 or 48 h following siRNA transfection. Viral RNA replication was measured after additional 24 h via nano-luciferase assays.

Immunoblotting

Whole-cell lysates were harvested in RIPA lysis buffer (Thermo Scientific) containing protease and phosphatase inhibitor cocktails. Protein concentration was measured using the detergent-compatible (BCA) protein assay (Thermo Scientific). Denatured lysates were separated on NuPage 8-16% Tris-glycine Midi Protein gels (Invitrogen) and transferred to polyvinylidene difluoride membrane (Immobilon) using a TransBlot Turbo dry transfer machine (Bio-Rad). The membrane was blocked and incubated with primary antibodies overnight at 4 °C followed by incubation with respective secondary antibodies and revealed with ECL Prime (Thermo). Chemiluminescent signals were acquired using Odyssey imaging system (Li-Cor), and densitometric analysis was performed using Image Studio 5.2 software (LI-COR, USA). All experiments were conducted and analyzed in 3–4 independent experiments.

Immunofluorescence and confocal microscopy. For detection of viral protein in ALOs, SARS-CoV-2-infected ALO-derived monolayers were washed with PBS, fixed with 4% PFA, blocked, and incubated with mouse mAb SARS-CoV-2 nucleocapsid antibody (SinoBiological) overnight at 4 °C, followed by incubation with secondary antibodies,

and counterstaining with DAPI (ThermoFisher). Images were taken on an SP8 microscope (Leica).

For colocalization and autophagy studies, A549-ACE2 cells were transduced with the Premo Autophagy Tandem Sensor RFP-GFP-LC3B kit (P36239, Thermo Scientific) and in 24 h, infected with SARS-CoV-2 (MOI = 0.5) for 2 h, followed by PBS washing and addition of medium containing 5 μM RMC-113, 5 μM apilimod, 10 μM chloroquine or DMSO. At 24 hpi, cells were fixed with 4% PFA, permeabilized with 0.5% (v/v) Triton-X-100, blocked with 2% (v/v) bovine serum albumin (BSA; Sigma-Aldrich) and stained as described above.

For imaging in siRNA-depleted cells, A549-ACE2 cells were transduced with premoRFP-GFP-LC3B sensor for 24 h and infected with WT SARS-CoV-2 for 2 h, washed with PBS, and replenished with the new medium. Images were acquired using LSM 710 confocal microscope (Zeiss).

To quantitate autophagic flux, image stacks were processed using 3D deconvolution in Zen 2.1 software. Maximum intensity projections of image stacks with both green and red channels were generated, and puncta counts for the respective channels were recorded using the Mosaic and ITCN plugins in Image J. Autolysosomal numbers were computed by subtracting the autophagosome count from the total puncta count, determined by combining the green and red channel image stacks using Fiji. For colocalization quantification, the JACoP plugin in Fiji was used, and Manders' correlation coefficients (M2) calculated.

Degradation assays

A549-ACE2 cells were transfected with a GFP-ORF3a and Gluc2-NSP3 expressing plasmid using Lipofectamine3000 transfection reagent. 48 h later, cells were treated with DMSO or RMC-113. Whole-cell lysates were harvested in RIPA lysis buffer at 0, 4-, 8-, 16- and 24 h post-treatment, followed by immunoblotting with anti-GFP and anti-actin antibodies. Protein half-life was calculated using GraphPad Prism software and Excel by fitting the curve with a one-exponential phase decay model, $\frac{\ln(2)}{K} = t_{1/2}$, here, K represents the rate constant, and ln(2) denotes the natural logarithm of 2.

In vitro kinase assays

In vitro kinase assays to determine IC_{50} and dissociation constant (K_d) were performed on the LabChip platform (Nanosyn) and Eurofins respectively.

NanoBRET assays were performed at Carna Biosciences. Briefly, HEK293 cells were transiently transfected with the NanoLuc® Fusion DNA and incubated at 37 °C. Twenty hours post-transfection, NanoBRET™ tracer reagent and the compounds were added to the cells and incubated at 37 °C for 2 h. Nanoluciferase-based bioluminescence resonance energy transfer (BRET) was measured using NanoBRET™ Nano-Glo® Substrate on a GloMax® Discover Multimode Microplate Reader (Promega).

Kinome profiling

Multiplexed Inhibitor Bead (MIB) affinity chromatography/MS analysis was performed as previously described[20]. Briefly, SUM159 cell lysates were incubated with either DMSO or the indicated concentration of RMC-113 and SRN2-002 for 30 min on ice. Kinase fragments were then detected and analyzed by mass spectrometry. The abundance of kinases was quantified in a label-free manner using MaxQuant software.

ProQinase assay was conducted by ProQinase (GmbH, Germany) by measuring residual activity of 335 wild-type protein kinases upon incubation with RMC-113 at 0.1 and 1 μM.

Molecular modeling

Molecular modeling was conducted with Maestro (Schrödinger Releases 2021-4/2022-2, Maestro, Schrödinger, LLC, New York, NY, 2021/2022) with OPLS4 force field[48]. Induced fit docking of SRN2-002 to MD simulation derived structures was conducted as reported earlier[49]. MD simulations of RMC-113 in complex with PIKfyve (PDB ID: 7K2V)[50] and PIP4K2C (8BQ4)[51] were run with Desmond[52], resulting in total aggregate simulation data of 72 and 20 μs, respectively (see details below).

Molecular dynamics simulations

To build the PIKfyve–RMC-113 complex, as no high-quality crystal structure of PIKfyve kinase domain was available, we used the cryo-EM structure (PDB ID: 7K2V)[50]. RMC-113 was manually placed on the binding site of PIKfyve utilizing the information of an analogue structure in complex with the lipid kinase PI3K p110δ (PDB ID: 2WXM)[53] (Schrödinger Release 2021-4). Next, the obtained protein–ligand complex structure was prepared with Protein Preparation Wizard[54]. The termini were capped, H-bonds were optimized, and system was energy minimized twice using 0.5 Å heavy atom RMSD convergence. The energy minimized system was solvated in a cubic box with a 15 Å minimum distance to the box edges from the protein or ligand atoms. We used TIP3P model[55] to describe the water and system was neutralized with six Cl^- ions and K^+ and Cl^- ions were added to obtain a final salt concentration of 0.15 M. The final system contained a total of 55,180 atoms. The default Desmond relaxation protocol was applied before the production simulations. The production simulations were run in NpT ensemble: 1.01325 bar, Nosé–Hoover method; 300 K, Martyna–Tobias–Klein method; RESPA integrator with 2, 2, and 6 fs timesteps for bonded, near and far, respectively; Coulombic cutoff of 9 Å. In total, we ran 20 replica simulations (Supplementary Table 1), each with a different random seed, with a length of 4 μs each. Within these final simulations, we discarded two replicas from further analysis due to their conformational instability. The remaining 18 replicas, with an aggregate simulation data of 72 μs, were used in the final analysis.

Building the PIP4K2C–RMC-113 complex, used a combination of X-ray structure 8BQ4[51] and AlphaFold model (AF-Q8TBX8-F1)[56] using (Schrödinger Release 2022-2). RMC-113 was superimposed over the co-crystallized ligand of 8BQ4 and the structure was directed to protein-ligand complex refinement protocol for local optimization of side chain conformations. A similar pose as to PIKfyve was gained. Missing loops of the template protein (residues Gly136–Gly139; Ile291–Phe350; Thr377–Thr402) were modelled with the assistance of Maestro's homology modelling tool, using multiple template approach i.e., consensus protocol, where chains A and B from 8BQ4 and AlphaFold[9] model AF-Q8TBX8-F1 were selected as input structures, respectively. As a result, a complete PIP4K2C kinase domain (residues 45-421) structure was obtained, where the core of the protein was taken from 8BQ4, and missing loops were obtained from AF-Q8TBX8-F1. The earlier obtained RMC-113 pose was merged to new model and the refinement step was repeated, after which the structure was H-bond optimized and minimized using standard Protein Preparation Wizard (as above). The energy minimized structure, was solvated with TIP3P waters in an orthorhombic periodic system with 10 Å buffer (91.0 × 77.9 × 71.2 Å), and neutralized, including 0.1 M NaCl buffer. The final system contained a total of 46,285 atoms. Desmond MD simulations were carried out using same settings as with PIKfyve, resulting in 10 replicas of with the length of 2 μs each (total simulation time of 20 μs) (Supplementary Table 1).

Simulation trajectories were analyzed by Maestro simulation interactions diagram tools and visualization of the structures was conducted with PyMOL (The PyMOL Molecular Graphics System, Version 2.5.4 Schrödinger, LLC.). H-bonds were defined as a 2.5 Å distance with ≥120° angle for a donor and ≥90° for an acceptor, and water bridged interactions were defined as 2.8 Å, ≥110° and ≥90°. The hydrophobic contact definition was 3.6 Å for non-specific hydrophobic interactions and 4.5 Å distance for π–cation or π–π interactions.

Target engagement by Click Chemistry

As described[22], cell lysates were prepared from A549-ACE-2 cells infected with SARS-CoV-2 at 24 hpi (MOI = 1). Lysis buffer containing 50 mM PIPES, 50 mM NaCl, 5 mM MgCl2, 5 mM EDTA, 0.5% NP-40, 0.1% Triton X-100, and 0.1% Tween 20 at pH 7.4 was used to inactivate the virus, followed by centrifugation to remove debris. For the biotin-azide-streptavidin magnetic pull-down, cell lysates were incubated with the photoaffinity clickable probe (SRN2-002, 1 and 5 μM), followed by UV light irradiation. A CuAAC click reaction mixture containing CuSO4, THPTA, Biotin-Azide, and sodium ascorbate was added, and after desalting, streptavidin magnetic beads were used to pull down biotin-protein complexes. The resulting product was washed and analyzed by immunoblotting. Controls included samples without the clickable probe, without UV irradiation, and with competitive click reactions using excess parent compound (RMC-113, 10X or 50X).

Lipid extraction, purification and methylation

A549-ACE2 cells infected with SARS-CoV-2 (MOI = 0.5) were treated with 5 μM RMC-113 or DMSO. Following cell lysis at 24 hpi, samples were inactivated using 1.5 ml methanol and mixed with chloroform (chloroform/methanol 1:9) supplemented with 1 nmol of $PI(4,5)P_2$ as an absorption inhibitor to prevent non-specific binding, along with 10 pmol each of 4 reference standards (deuterated 5 PI, deuterated 62 PI3P, deuterated 62 $PI(4,5)P_2$) spiked into methanol. The mixture was inactivated with 1.5 ml methanol and chloroform, followed by addition of Ultrapure water, 2 M HCl, and 1 M NaCl. The crude lipid extract (2.9 ml) was subjected to purification using a DEAE Sepharose Fast Flow column, washed with chloroform/methanol (1:1) and chloroform/methanol/28% aqueous ammonia/glacial acetic acid (200:100:3:0.9), and then eluted with chloroform/methanol/12 M hydrochloric acid/ultrapure water (12:12:11). The eluate was combined with 850 μl of 120 mM NaCl and purified by centrifugation. The resulting purified phosphoinositides underwent derivatization through methylation by adding 0.6 M trimethylsilyl diazomethane at room temperature for 10 minutes. The reaction was quenched with 20 μl of glacial acetic acid. The samples were further processed with methanol/ultrapure water/chloroform (48:47:3), followed by evaporation under nitrogen and dissolution in 100 μl of acetonitrile for analysis. Samples were placed on a shaker for 10 minutes and then transferred to a 200 μl glass vial insert. Samples were loaded on a UPLC autosampler and injected at 30 μl for LC/MS analysis.

Lipidomics analysis

These experiments were conducted at Element Materials Technology. Purified, methylated lipid samples were analyzed using posphoinositide regioisomer measurement by chiral column chromatography coupled with tandem mass spectrometry (PRMC-MS), employing an MS triple quad Sciex Qtrap 5500 mass spectrometer operating in positive ion mode. Mass spectra were acquired over a broad m/z range (5–2000), with multiple reaction monitoring (MRM) applied for targeted data acquisition. Instrument parameters, including ionization voltages (5.5 kV), collision energy (30–42 V), gas pressures (20 psi for curtain gas, 9 psi for collision gas, and 30 psi for ion source gases), and temperature (400 °C source block temperature), were meticulously optimized to maximize sensitivity and resolution. Liquid chromatography (LC) separation was achieved using a Lux 3 μm i-Cellulose-5 column (250 × 4.6 mm) maintained at 35 °C, with a mobile phase gradient of methanol/5 mM ammonium acetate (A) and acetonitrile/5 mM ammonium acetate (B). The LC gradient started at 0% A and 100% B, transitioning to 30% A and 70% B over 3 min, held for 15 min, and then re-equilibrated. Data processing involved normalization against deuterated reference standards, enabling precise quantification and comparison of lipid species across samples.

virus-inclusive single cell RNA-seq (ViscRNA-seq)

ALOs were seeded in 96-well plates at 1×10^5 cells per well and infected with SARS-CoV-2 (MOI = 1) in the presence of 5 μM RMC-113 or 0.1% DMSO. After a 4 h incubation, the viral inoculum was removed, and cells were washed thoroughly and supplemented with fresh medium with or without the compound. At 4 and 24 hpi, ALOs were washed and then detached via 5 min incubation with TrypLE followed by centrifugation at 300 g for 10 min. The pellets were suspended and fixed with Cell fixation solution (Parse, Evercode Fixation, cat: ECF2001, Part number WF303) for 10 min followed by incubation with Cell permeabilization Solution (Parse, Evercode Fixation, cat: ECF2001, Part number WF305) for 3 min at RT. ALOs were then taken out from BSL3 for single-cell sequencing according to the manufacturer's instructions (Parse, EvercodeTM WT mini Mega v2).

viscRNA-seq data analysis

Data processing. The Parse Biosciences processing pipeline (splitpipe v1.0.3a) was used with default settings to align the raw sequencing reads to the Parse Biosciences pre-built human reference (GRCh38) and to demultiplex samples. The downstream processing was performed using the Python package Scanpy[57]. Cells with more than 30% mitochondrial reads or more than 50,000 unique molecular identifiers (UMIs) were excluded from subsequent analysis. The raw gene counts matrix was normalized to a total UMI counts of 1,000,000 (CPM) per cell and was log2 transformed with the addition of a pseudocount of 1.

Cell clustering and annotation. Samples from three independent experiments were clustered and annotated separately. Principal component analysis (PCA) was performed on the 2000 features that were highly variable across most of the samples. The first 50 PCA components were used to generate the nearest neighbor graphs and were subjected to a non-linear dimensionality reduction using Uniform Manifold Approximation and Projection (UMAP). Cells were clustered using the Leiden algorithm with a resolution of 1. Cell clusters were annotated based on the expression of marker genes as follows: (1) AT2-like cells (SFTPD, MUC1, CLIC5), (2) AT1-like cells (HOPX, RTKN2, EMP2, CAV1), (3) Basal-like cells (NGFR, ITGA6, TP63, KRT5), and (4) transitioning cells that are HOPX and NGFR negative and CEACAM6 positive. After initial annotation, PCA components were computed on the 2,000 features that were highly expressed across all the samples from independent experiments. Principal components were adjusted for each sample using Harmony integrate function. The first 40 Harmony components were used to generate batch-corrected UMAP visualizations.

Detection of viral RNA harboring cells (VHCs). To capture the viral RNAs in SARS-CoV-2 infected samples, the raw sequencing reads were aligned to a custom reference genome by integrating the SARS-CoV-2 isolate USA-WA1/2020 (MT246667.1) to the human reference genome (GRCh38) using the Parse Biosciences processing pipeline as described above. Reads uniquely mapped to the viral genome were extracted as viral reads. Cells with at least four detected viral transcripts were considered as VHCs, and cells with zero detected viral transcripts were considered as bystanders. This threshold was defined empirically based on the inflection point in the cumulative distribution of viral RNA counts across cells in each sample.

Pairwise comparison of VHCs and bystanders. Both VHCs and bystanders were subsampled randomly to the lowest number of cells in one group and log2 fold change of the gene expression was calculated. This calculation was iterated 100 times to form an empirical distribution of differential expression. The median log2 fold change of all the comparisons was used to estimate effect size (color) and the noise level (box size) of the comparison was shown using boxplots.

Protein-fragment complementation assays. Combinations of plasmids encoding prey (A) and bait (B) proteins, each fused to a fragment of the Gaussia luciferase protein (GLuc1 and GLuc2) or control vectors, were co-transfected into HEK-293T cells plated in 96-well plates in triplicate[35]. At 24 h post-transfection, cells were lysed and subjected to luciferase assays (Promega). Results were expressed as NLRs calculated as follows: the average signal in cells transfected with GLuc1-A and GLuc2-B was divided by the average signal in wells transfected with GLuc1-A and an empty GLuc2 vector and those transfected with GLuc2-B and an empty GLuc1 vector.

Statistical analysis

Data were analyzed with GraphPad Prism software. EC_{50} and CC_{50} values were measured by fitting of data to a 3-parameter logistic curve. *P* values were calculated by 1-way ANOVA with either Dunnett's or Tukey's multiple comparisons tests or a two-sided Wilcoxon test with Benjamini-Hochberg correction as specified in each figure legend.

Reporting summary

Further information on research design is available in the Nature Portfolio Reporting Summary linked to this article.

Data availability

PDB coordinates of the representative snapshots shown in Fig. 2 are provided in Supplementary Table 1. Full trajectories of the Desmond molecular dynamics simulations are freely available at: https://doi.org/10.5281/zenodo.10878041 (PIKfyve simulations) and https://doi.org/10.5281/zenodo.10889319 (PIP4K2C simulations). Data related to viscRNA-seq have been deposited in the NCBI Gene Expression Omnibus (GEO) and are accessible through GEO accession number GSE272840. The code used in the present study is publicly available at https://github.com/hbusra/ALO-scRNAseq-data-analysis. Lipidomics data are available at the metabolomics workbench database under accession code Study ID ST003388 (DatatrackID:5007). The processed lipidomics data are available at https://doi.org/10.21228/M89C1V. Source data are available at https://doi.org/10.6084/m9.figshare.29260706.

References

1. Weaver, S. C., Ferro, C., Barrera, R., Boshell, J. & Navarro, J.-C. Venezuelan equine encephalitis. *Annu. Rev. Entomol.* **49**, 141–174 (2004).
2. Karim, M., Lo, C.-W. & Einav, S. Preparing for the next viral threat with broad-spectrum antivirals. *J. Clin. Investig.* **133**, e170236 (2023).
3. Llorente, A., Arora, G. K., Grenier, S. F. & Emerling, B. M. PIP kinases: a versatile family that demands further therapeutic attention. *Adv. Biol. Regul.* **87**, 100939 (2023).
4. Sbrissa, D., Ikonomov, O. C. & Shisheva, A. PIKfyve, a mammalian ortholog of yeast Fab1p lipid kinase, synthesizes 5-phosphoinositides: effect of insulin. *J. Biol. Chem.* **274**, 21589–21597 (1999).
5. Sharma, G. et al. A family of PIKFYVE inhibitors with therapeutic potential against autophagy-dependent cancer cells disrupt multiple events in lysosome homeostasis. *Autophagy* **15**, 1694–1718 (2019).
6. Sands, B. E. et al. Randomized, double-blind, placebo-controlled trial of the oral interleukin-12/23 inhibitor apilimod mesylate for treatment of active Crohn's disease. *Inflamm. Bowel Dis.* **16**, 1209–1218 (2010).
7. Kang, Y.-L. et al. Inhibition of PIKfyve kinase prevents infection by Zaire ebolavirus and SARS-CoV-2. *Proc. Natl. Acad. Sci. USA* **117**, 20803–20813 (2020).
8. Huang, P.-T., Einav, S. & Asquith, C. R. PIKfyve: a lipid kinase target for COVID-19, cancer and neurodegenerative disorders. *Nat. Rev. Drug Discov.* **20**, 730 (2021).
9. Rameh, L. E., Tolias, K. F., Duckworth, B. C. & Cantley, L. C. A new pathway for synthesis of phosphatidylinositol-4, 5-bisphosphate. *Nature* **390**, 192–196 (1997).
10. Lundquist, M. R. et al. Phosphatidylinositol-5-phosphate 4-kinases regulate cellular lipid metabolism by facilitating autophagy. *Mol. Cell* **70**, 531–544. e539 (2018).
11. Al-Ramahi, I. et al. Inhibition of PIP4Kγ ameliorates the pathological effects of mutant huntingtin protein. *Elife* **6**, e29123 (2017).
12. Vicinanza, M. et al. PI (5) P regulates autophagosome biogenesis. *Mol. cell* **57**, 219–234 (2015).
13. Metz, P. et al. Dengue virus inhibition of autophagic flux and dependency of viral replication on proteasomal degradation of the autophagy receptor p62. *J. Virol.* **89**, 8026–8041 (2015).
14. Jones-Jamtgaard, K. N., Wozniak, A. L., Koga, H., Ralston, R. & Weinman, S. A. Hepatitis C virus infection increases autophagosome stability by suppressing lysosomal fusion through an Arl8b-dependent mechanism. *J. Biol. Chem.* **294**, 14257–14266 (2019).
15. Zhang, Y. et al. The SARS-CoV-2 protein ORF3a inhibits fusion of autophagosomes with lysosomes. *Cell Discov.* **7**, 31 (2021).
16. Sun, X. et al. SARS-CoV-2 non-structural protein 6 triggers NLRP3-dependent pyroptosis by targeting ATP6AP1. *Cell Death Differ.* **29**, 1240–1254 (2022).
17. Wouters, R. et al. Cyclin G-associated kinase (GAK) affinity and antiviral activity studies of a series of 3-C-substituted isothiazolo [4, 3-b] pyridines. *Eur. J. Medicinal Chem.* **163**, 256–265 (2019).
18. Tindle, C. et al. Adult stem cell-derived complete lung organoid models emulate lung disease in COVID-19. *Elife* **10**, e66417 (2021).
19. Saul, S. et al. Anticancer pan-ErbB inhibitors reduce inflammation and tissue injury and exert broad-spectrum antiviral effects. *J. Clin. Investig.* 133, e169510 (2023).
20. Asquith, C. R. et al. Identification and optimization of 4-anilinoquinolines as inhibitors of cyclin G associated kinase. *ChemMedChem* **13**, 48–66 (2018).
21. Vasta, J. D. et al. Quantitative, wide-spectrum kinase profiling in live cells for assessing the effect of cellular ATP on target engagement. *Cell Chem. Biol.* **25**, 206–214. e211 (2018).
22. Simon, G. M., Niphakis, M. J. & Cravatt, B. F. Determining target engagement in living systems. *Nat. Chem. Biol.* **9**, 200–205 (2013).
23. De Vivo, M., Masetti, M., Bottegoni, G. & Cavalli, A. Role of molecular dynamics and related methods in drug discovery. *J. Medicinal Chem.* **59**, 4035–4061 (2016).
24. Manz, T. D. et al. Discovery and structure–activity relationship study of (Z)-5-methylenethiazolidin-4-one derivatives as potent and selective pan-phosphatidylinositol 5-phosphate 4-kinase inhibitors. *J. Medicinal Chem.* **63**, 4880–4895 (2020).
25. Lima, K. et al. The PIP4K2 inhibitor THZ-P1-2 exhibits antileukemia activity by disruption of mitochondrial homeostasis and autophagy. *Blood Cancer J.* **12**, 151 (2022).
26. Morioka, S. et al. A mass spectrometric method for in-depth profiling of phosphoinositide regioisomers and their disease-associated regulation. *Nat. Commun.* **13**, 83 (2022).
27. Fahnøe, U. et al. Versatile SARS-CoV-2 reverse-genetics systems for the study of antiviral resistance and replication. *Viruses* **14**, 172 (2022).
28. Williams, J. M., Chen, Y.-J., Cho, W. J., Tai, A. W. & Tsai, B. Reticulons promote formation of ER-derived double-membrane vesicles that facilitate SARS-CoV-2 replication. *J. Cell Biol.* **222**, e202203060 (2023).
29. Gassen, N. C. et al. SARS-CoV-2-mediated dysregulation of metabolism and autophagy uncovers host-targeting antivirals. *Nat. Commun.* **12**, 3818 (2021).
30. Shang, C. et al. Inhibition of autophagy suppresses SARS-CoV-2 replication and ameliorates pneumonia in hACE2 transgenic mice and xenografted human lung tissues. *J. Virol.* **95**,e0153721 (2021).

31. Mauthe, M. et al. Chloroquine inhibits autophagic flux by decreasing autophagosome-lysosome fusion. *Autophagy* **14**, 1435–1455 (2018).
32. Liu, L. et al. Chloroquine inhibits cell growth in human A549 lung cancer cells by blocking autophagy and inducing mitochondrial-mediated apoptosis. *Oncol. Rep.* **39**, 2807–2816 (2018).
33. Zanini, F., Pu, S.-Y., Bekerman, E., Einav, S. & Quake, S. R. Single-cell transcriptional dynamics of flavivirus infection. *Elife* **7**, e32942 (2018).
34. Hung, S.-T., et al. PIKFYVE inhibition mitigates disease in models of diverse forms of ALS. *Cell* **186**, 786–802 (2023).
35. Schor, S. et al. The cargo adapter protein CLINT1 is phosphorylated by the Numb-associated kinase BIKE and mediates dengue virus infection. *J. Biol. Chem.* **298**, 101956 (2022).
36. Poli, A. et al. Phosphatidylinositol 5 phosphate (Pi5p): from behind the scenes to the front (nuclear) stage. *Int. J. Mol. Sci.* **20**, 2080 (2019).
37. Clausen, T. H. et al. p62/SQSTM1 and ALFY interact to facilitate the formation of p62 bodies/ALIS and their degradation by autophagy. *Autophagy* **6**, 330–344 (2010).
38. McEwan, D. G. et al. PLEKHM1 regulates autophagosome-lysosome fusion through HOPS complex and LC3/GABARAP proteins. *Mol. Cell* **57**, 39–54 (2015).
39. Jiao, Y. et al. PABPC4 broadly inhibits coronavirus replication by degrading nucleocapsid protein through selective autophagy. *Microbiol. Spectr.* **9**, e00908–e00921 (2021).
40. Nishitsuji, H., Iwahori, S., Ohmori, M., Shimotohno, K. & Murata, T. Ubiquitination of SARS-CoV-2 NSP6 and ORF7a facilitates NF-κB activation. *MBio* **13**, e00971–00922 (2022).
41. Logue, J. et al. PIKfyve-specific inhibitors restrict replication of multiple coronaviruses in vitro but not in a murine model of COVID-19. *Commun. Biol.* **5**, 808 (2022).
42. Ikonomov, O. C., Sbrissa, D. & Shisheva, A. Small molecule PIKfyve inhibitors as cancer therapeutics: Translational promises and limitations. *Toxicol. Appl. Pharmacol.* **383**, 114771 (2019).
43. Arora, G. K., Palamiuc, L. & Emerling, B. M. Expanding role of PI5P4Ks in cancer: a promising druggable target. *FEBS Lett.* **596**, 3–16 (2022).
44. Karim, M. et al. Numb-associated kinases are required for SARS-CoV-2 infection and are cellular targets for antiviral strategies. *Antivir. Res.* **204**, 105367 (2022).
45. Zou, G., Xu, H. Y., Qing, M., Wang, Q.-Y. & Shi, P.-Y. Development and characterization of a stable luciferase dengue virus for high-throughput screening. *Antivir. Res.* **91**, 11–19 (2011).
46. Spiteri, G. et al. First cases of coronavirus disease 2019 (COVID-19) in the WHO European Region, 24 January to 21 February 2020. *Eurosurveillance* **25**, 2000178 (2020).
47. Karim, M., Pohane, A. A., Lo, C.-W., Einav, S. & Garhyan, J. Chemical inactivation strategies for SARS-CoV-2-infected cells and organoids. *STAR Protoc.* **5**, 102906 (2024).
48. Lu, C. et al. OPLS4: Improving force field accuracy on challenging regimes of chemical space. *J. Chem. Theory Comput.* **17**, 4291–4300 (2021).
49. Kircher, T. et al. Design and synthesis of novel fluorescently labeled analogs of vemurafenib targeting MKK4. *Eur. J. Medicinal Chem.* **209**, 112901 (2021).
50. Lees, J. A., Li, P., Kumar, N., Weisman, L. S. & Reinisch, K. M. Insights into lysosomal PI (3, 5) P2 homeostasis from a structural-biochemical analysis of the PIKfyve lipid kinase complex. *Mol. Cell* **80**, 736–743. e734 (2020).
51. Rooney, T. P. et al. The identification of potent, selective, and brain penetrant pi5p4kγ inhibitors as in vivo-ready tool molecules. *J. Medicinal Chem.* **66**, 804–821 (2022).
52. Bowers, K. J. et al, Molecular dynamics—Scalable algorithms for molecular dynamics simulations on commodity clusters, presented at SC '06: International Conference for High Performance Computing, Networking, Storage and Analysis, Tampa, Florida (2006).
53. Berndt, A. et al. The p110δ structure: mechanisms for selectivity and potency of new PI (3) K inhibitors. *Nat. Chem. Biol.* **6**, 117–124 (2010).
54. Madhavi Sastry, G., Adzhigirey, M., Day, T., Annabhimoju, R. & Sherman, W. Protein and ligand preparation: parameters, protocols, and influence on virtual screening enrichments. *J. Computer-aided Mol. Des.* **27**, 221–234 (2013).
55. Jorgensen, W. L., Chandrasekhar, J., Madura, J. D., Impey, R. W. & Klein, M. L. Comparison of simple potential functions for simulating liquid water. *J. Chem. Phys.* **79**, 926–935 (1983).
56. Jumper, J. et al. Highly accurate protein structure prediction with AlphaFold. *Nature* **596**, 583–589 (2021).
57. Wolf, F. A., Angerer, P. & Theis, F. J. SCANPY: large-scale single-cell gene expression data analysis. *Genome Biol.* **19**, 1–5 (2018).

Acknowledgements

This work was supported by grant 1R01AI158569-01 from the NIH (to SE), awards HDTRA11810039 from the Defense Threat Reduction Agency/Fundamental Research to Counter Weapons of Mass Destruction (to SE, SDJ) and W81XWH2210283 and W81XWH-16-1-0691 from the Department of Defense/Congressionally Directed Medical Research Programs (to SE and SDJ), and grants 3R01DK107585-05S1 and UCOP-R00RG2642 (to SD). SE is a Chan Zuckerberg Biohub investigator. This work was partly supported by the NIH Common Fund Illuminating the Druggable Genome (IDG) program (NIH Grant U24DK116204) (CRMA, GLJ, ME) and The Academy of Finland PROFI6 program (CRMA). MK was supported by a PhRMA Foundation Postdoctoral Fellowship in Translational Medicine and NIH T32 training grant (5T32AI007502-27). MM was supported by the Stanford Pandemic Preparedness Hub Fellowship. LG was supported by a long-term European Molecular Biology Organization Fellowship (ALTF584-2021). Microscopy and mass-spectrometry were done on instruments in the Cell Sciences Imaging Core Facility (RRID:SCR_017787, LSM780 confocal/multiphoton) and Thermo Exactive Orbitrap LC/MS system (RRID:SCR_018700), respectively. We thank the investigators who provided plasmids and compounds (see Methods). We thank the Stanford BSL3 service center and Jaishee Garhyan (director) for their assistance in the BSL3. We thank Biocenter Finland/DDCB for financial support and CSC – IT Center for Science, Finland, for computational resources. Part of this research work was performed using the 'Caps-It' research infrastructure (project ZW13-02) that was financially supported by the Hercules Foundation (FWO) and Rega Foundation, KU Leuven. We thank UC San Diego, HUMANOID™ for ALOs. We thank the Stanford Clinical Virology Laboratory's staff for their help with sequencing. Opinions, conclusions, interpretations, and recommendations are those of the authors and are not necessarily endorsed by the funders. The mention of trade names or commercial products does not constitute endorsement or recommendation for use by the Department of the Army or the Department of Defense. BioRender software was used for the preparation of some illustrations.

Author contributions

M.K., M.M., C.W.L., S.S., H.B.C., M.G., L.G., A.O., D.H.N.T., A.A., C.M., M.P.E., K.A.G., M.K.S., N.A.M., and C.A.C. designed and performed the experiments and conducted data analysis. S.D., J.B., J.G., provided reagents and guidance. S.E., C.R.M.A., S.D.J., G.L.J., P.L., J.N., W.C., J.D., N.N., P.K.J., B.A.P., T.L., T.P., A.P., and F.Z. provided scientific oversight and guidance. M.K., S.E., C.R.M.A., and M.M. wrote the first version of the manuscript. S.E., C.R.M.A., and S.D.J. provided funding for the studies.

Competing interests

The authors declare no competing interests.

Additional information

Supplementary information The online version contains supplementary material available at https://doi.org/10.1038/s41467-025-61759-1.

Correspondence and requests for materials should be addressed to Shirit Einav.

Peer review information *Nature Communications* thanks the anonymous, reviewer(s) for their contribution to the peer review of this work. A peer review file is available.

[1]Department of Medicine, Division of Infectious Diseases and Geographic Medicine, Stanford University, Stanford, CA, USA. [2]Department of Pharmacology, School of Medicine, University of North Carolina at Chapel Hill, Chapel Hill, NC, USA. [3]Department of Infectious Diseases, University of Copenhagen, Copenhagen, Denmark. [4]Copenhagen Hepatitis C Program (CO-HEP), Department of Infectious Diseases, Copenhagen University Hospital–Hvidovre, Hvidovre, Denmark. [5]Copenhagen Hepatitis C Program (CO-HEP), Department of Immunology and Microbiology, Faculty of Health and Medical Sciences, University of Copenhagen, Copenhagen, Denmark. [6]Department of Pathology, Stanford University School of Medicine, Stanford, CA, USA. [7]Baxter Laboratory, Department of Microbiology & Immunology. Stanford University School of Medicine, Stanford, CA, USA. [8]Lineberger Comprehensive Cancer Center, University of North Carolina School of Medicine, Chapel Hill, NC, USA. [9]Biomedical & Nutritional Science, Center for Pathogen Research & Training (CPRT), University of Massachusetts-Lowell, Lowell, USA. [10]KU Leuven, Department of Microbiology, Immunology and Transplantation, Rega Institute for Medical Research, Laboratory of Virology and Chemotherapy, Leuven, Belgium. [11]US Army Medical Research Institute of Infectious Diseases, Viral Immunology Branch, Frederick, MD, USA. [12]Chan Zuckerberg Biohub, San Francisco, CA, USA. [13]School of Pharmacy, Faculty of Health Sciences, University of Eastern Finland, Kuopio, Finland. [14]School of Clinical Medicine, UNSW Sydney, Sydney, NSW, Australia. [15]Cellular Genomics Futures Institute, UNSW Sydney, Sydney, NSW, Australia. [16]Evolution and Ecology Research Centre, UNSW Sydney, Sydney, NSW, Australia. [17]Department of Microbiology and Immunology, Stanford University, Stanford, CA, USA. [18]These authors contributed equally: Marwah Karim, Manjari Mishra. ✉e-mail: seinav@stanford.edu